Electronic Supplementary Information (ESI)

Water vapour induced structural flexibility in a square lattice coordination network

Kyriaki Koupepidou, Andrey A. Bezrukov, Dominic C. Castell, Debobroto Sensharma, Soumya Mukherjee and Michael J. Zaworotko*

Bernal Institute, Department of Chemical Sciences, University of Limerick, Limerick V94 T9PX, Republic of Ireland.

Table of Contents

Methods

S1. Materials and Synthesis

The linker 1,3-bis(imidazol-1-yl)benzene (1,3-bib) was synthesized with modified reported procedures.[1] Other reagents and solvents were commercially available and were used without further purification.

Synthesis of 1,3-bib. 1,3-dibromobenzene (5.0 g, 21.2 mmol, 1.0 eq), CuI (0.8 g, 20 mol%), imidazole (4.33 g, 63.6 mmol, 3.0 eq) and K_2CO_3 (8.78 g, 63.6 mmol, 3.0 eq) were all added to anhydrous DMF (50 mL) under N_2. The resulting reaction mixture was then heated to 150 °C for 48 h under an atmosphere of N_2. After cooling to room temperature, the mixture was diluted with DCM (250 mL) and filtered. The filtered organic layer was transferred to a large separating funnel and washed twice with H_2O (2 × 500 mL). After drying over $MgSO_4$, the organic layer was concentrated under reduced pressure. Final purification was achieved by rapid trituration of the compound from a DCM/hexane mixture, affording 1,3-bib as an off-white solid (4.06 g, 91%). All characterization data matches well with literature reported values.[2]

Synthesis of sql-(1,3-bib)(ndc)-Ni-α ($[Ni_2(1,3\text{-bib})_3(ndc)_2(H_2O)_2]\cdot(DMA)5(H_2O)$). A mixture of $Ni(NO_3)_2\cdot6H_2O$ (29 mg, 0.1 mmol), 1,3-bib (11 mg, 0.05 mmol), ndc (12 mg, 0.05 mmol) and DMA/H_2O (6/2 mL) was added to a 28 mL glass vial. The vial was capped tightly, ultrasonicated for 5 minutes and then placed in an oven at 105 °C. After 24 hours, the vial was removed from the oven and allowed to cool to room temperature. Blue block shaped crystals were harvested by filtration and washed with DMA. Yield: 96% (based on ndc). Elemental analysis: calculated for $C_{64}H_{65}N_{13}Ni_2O_{16}$: C, 55.31%; H, 4.71%; N, 13.10%. Found: C, 54.72%; H, 4.20%; N, 12.85%.

Synthesis of sql-(1,3-bib)(ndc)-Ni-γ ($[Ni_2(1,3\text{-bib})_3(ndc)_2(H_2O)_2]\cdot4(MeOH)(H_2O)$). The as-synthesized **sql-(1,3-bib)(ndc)-Ni-α** was soaked in anhydrous methanol. The solvent was replaced 3 times over 1 day, and the sample was filtered to obtain **sql-(1,3-bib)(ndc)-Ni-γ**. Elemental analysis: calculated for $C_{64}H_{64}N_{12}Ni_2O_{15}$: C, 56.58%; H, 4.75%; N, 12.37%. Found: C, 57.28%; H, 3.75%; N, 13.22%.

Synthesis of sql-(1,3-bib)(ndc)-Ni-β ($[Ni_2(1,3\text{-bib})_3(ndc)_2(H_2O)_2]\cdot3(H_2O)$). The narrow-pore phase **sql-(1,3-bib)(ndc)-Ni-β** was obtained by heating the α phase at 60 °C under vacuum for 2 h. Elemental analysis: calculated for $C_{60}H_{52}N_{12}Ni_2O_{13}$: C, 56.90%; H, 4.14%; N, 13.27%. Found: C, 56.53%; H, 3.92%; N, 12.90%.

Synthesis of sql-(1,3-bib)(ndc)-Ni-α' ($[Ni_2(1,3\text{-bib})_3(ndc)_2(H_2O)_2]\cdot8(H_2O)$). The water-loaded **sql-(1,3-bib)(ndc)-Ni-α'** phase was obtained by soaking **sql-(1,3-bib)(ndc)-Ni-β** in water for 1 day. The sample was filtered to obtain **sql-(1,3-bib)(ndc)-Ni-α'**. Elemental analysis: calculated for $C_{60}H_{62}N_{12}Ni_2O_{18}$: C, 53.12%; H, 4.61%; N, 12.39%. Found: C, 53.90%; H, 3.54%; N, 12.73%.

S2. CSD and ToposPro TTO Database Search

S2A. CSD Database Search

The ConQuest function in the Cambridge Structural Database (CSD)[3] was implemented in order to examine the conformational differences between 1,3-bis(imidazol-1-yl)benzene (1,3-bib) and 1,4-bis(imidazol-1-yl)benzene (1,4-bib) in coordination compounds (0D, 1D, 2D, 3D). Two separate searches were conducted for each ligand bound to two metals. In each search the parameters examined were: (i) torsion angle between the imidazole ring and the central phenyl ring, (ii) metal-to-metal (M-M) distance and (iii) the carbon-to-carbon (C-C) distance between carbon atoms at the 2- position of the imidazole rings. These parameters are summarised in Figure S2 and the results of the search are shown in Figures S3 and S4.

S2B. ToposPro TTO Database Search

A survey using the ToposPro[4] Topological Types Observed (TTO) database was performed on coordination networks (1D, 2D, 3D) sustained by 1,3-bis(imidazol-1-yl)benzene (1,3-bib) and 1,4-bis(imidazol-1-yl)benzene (1,4-bib). The list of refcodes obtained was matched with topologies reported in the TOPOS TTO database (version: Dec 2021) using a custom-written Python script. Valence-bonded MOF topology determinations in either the standard or cluster representation were used.

S3. Topological Analysis

Topological analysis was conducted using the program ToposPro[4] (version 5.4.3.0).

Report:

```
#########################
1: [C30H23N6NiO5] [+ solvent]
#########################
Topology for ZA1
-------------------
Atom ZA1 links by bridge ligands and has
Common vertex with                    R(A-A)
ZA 1   0.3196   0.5846   0.4201  ( 1 0 0)   7.930A      1
ZA 1   0.8196   0.9154  -0.0799  ( 1 1-1)  11.278A      1
ZA 1   0.8196   0.9154   0.9201  ( 1 1 0)  11.278A      1
ZA 1   1.3196   0.5846   0.4201  ( 2 0 0)  14.044A      1
-------------------------
Structural group analysis
-------------------------
Structural group No 1
-------------------------
Structure consists of layers ( 0 1 0) with ZA
Num. groups=2; Thickness=7.24; Distances to Neighbors=7.310; 7.310

Coordination sequences
----------------------
ZA1:  1  2  3  4  5  6   7   8   9  10
Num   4  8 12 16 20 24  28  32  36  40
Cum   5 13 25 41 61 85 113 145 181 221
----------------------
TD10=221
Vertex symbols for selected sublattice
--------------------------------------
ZA1 Point symbol: [4^4 .6^2]
Extended point symbol:[4.4.4.4.6(2).6(2)]
--------------------------------------
Point symbol for net: [4^4.6^2]
4-c net; uninodal net

Topological type: sql (topos&RCSR.ttd) [4^4.6^2] - VS [4.4.4.4.*.*] (17896 types in 4 databases)
Elapsed time: 4.99 sec.
```

S4. Single-crystal X-ray Diffraction Measurements

S4A. General Procedure

Suitable single crystals of **sql-(1,3-bib)(ndc)-Ni-α**, **sql-(1,3-bib)(ndc)-Ni-β**, **sql-(1,3-bib)(ndc)-Ni-γ** and **sql-(1,3-bib)(ndc)-Ni-α'** were chosen for single-crystal X-ray diffraction measurements. Diffraction data were collected at 150 K on a Bruker D8 Quest diffractometer equipped with a MoKα microfocus source (λ = 0.7107 Å) and a Photon 100 detector. In all cases, data was indexed, integrated and scaled in APEX4.[5] Absorption correction was performed by multi-scan method using in SADABS.[6] Space group determination was performed simultaneously with structure solution using SHELXT intrinsic phasing methods and the solution was refined on F2 using SHELXL non-linear least squares implemented in Olex2 v1.2.10.[7] Anisotropic thermal parameters were applied to all non-hydrogen atoms. All the hydrogen atoms were generated geometrically. X-ray experimental data and refinement parameters are given in Table S2. The final crystal structures have been deposited in the Cambridge Crystallographic Data Centre (CCDC 2288421-2288425).

For the investigation of **sql-(1,3-bib)(ndc)-Ni-β** under activation conditions, a single crystal of **sql-(1,3-bib)(ndc)-Ni-β** was glued on a glass rod and placed in a sealed capillary. The capillary was then heated at 60 ˚C under vacuum overnight. After this, the heating was turned off and the crystal was kept under dynamic vacuum for two additional days. The capillary was then flame sealed under dynamic vacuum and a SXCRD experiment was performed at 150 K on a Bruker D8 Quest diffractometer equipped with a MoKα microfocus source (λ = 0.7107 Å) and a Photon 100 detector. The data was indexed as described above, and the results are shown in Table S2. An additional experiment was performed following a similar procedure but heating was increased to 100 ˚C. When this crystal was placed on the diffractometer, no diffraction pattern was observed, indicating that the sample had decomposed after heating at this temperature.

All crystals show twinning and the appropriate twin law was applied in each case. The guest accessible space for all compounds was calculated without removing the hydrogen bonded water molecule (Figure S10), as it remains as part of the framework even during activation conditions.

S4B. Specific Refinement Details

The structures reported in this manuscript are all coordination network structures with guest accessible space and moderate degree of porosity. The accessible space is occupied in each case by guest molecules, such as *N,N*-Dimethylacetamide (DMA), methanol or water. In all cases were water was present, hydrogen atoms were not added unless a visible electron density was found to support the evidence and directionality of the O-H bond. In all the other cases, hydrogen atoms were omitted but must be considered as being present and were therefore included in the chemical moiety formulae. In most cases the second hydrogen atom of the hydrogen bonded hydrate molecule (Figure S12) was not located. Additionally, all

crystals selected were inversion twins, so the appropriate twin law refinement was performed on the raw data.

Specific refinement details and alerts:

sql-(1,3-bib)(ndc)-Ni-γ. Half a hydrogen bonded water molecule per Ni unit was successfully modelled. In addition, four methanol positions per Ni unit were found and refined with free occupancy, but the rest of the methanol molecules could not be accurately positioned due to high degree of disorder. The data was treated with the SQUEEZE routine in Olex2 to account for the residual electron density. The electron count/Ni unit agreed with the presence of 1.5 additional methanol molecules (electron count/formula unit = 28, 28/18 = 1.56).

Alert Level B

PLAT341_ALERT_3_B Low Bond Precision on C-C Bonds ..... 0.01585 Ang.

Response: **sql-(1,3-bib)(ndc)-Ni-gamma** was prepared by exchanging the as-synthesized sample **sql-(1,3-bib)(ndc)-Ni-alpha** with methanol, which triggered a structural transformation. As a result, the crystal quality was impacted. This was reflected in a B level alert related to low bond precision, which we attribute to poor diffraction. The reduced crystal quality of this sample can also be attributed to the fact that the crystals are susceptible to losing methanol solvate molecules and simultaneously adsorbing water molecules from the atmosphere.

PLAT430_ALERT_2_B Short Inter D...A Contact O3 ..O1C . 2.79 Ang.
x,y,z = 1_555 Check

Response: The atom O1C belongs to a guest methanol molecule in **sql-(1,3-bib)(ndc)-Ni-gamma**, which has a corresponding carbon atom named C1C. C1C is hydrogen bonded to the O3 atom belonging to an ndc ligand, therefore causing a short intermolecular distance.

sql-(1,3-bib)(ndc)-Ni-β. One H_2O guest molecule per Ni unit was successfully modelled. The rest of the water molecules could not be accurately positioned due to high degree of disorder. The data was treated with the SQUEEZE routine in Olex2 to account for the residual electron density. The electron count/Ni unit agreed with the presence of 0.4 additional hydrate molecule (electron count/formula unit = 4, 4/10 = 0.40).

sql-(1,3-bib)(ndc)-Ni-β_vacuum. For this experiment, a single crystal of **sql-(1,3-bib)(ndc)-Ni-β** was glued on a glass rod in a sealed capillary, and subsequently heated again under vacuum (please see experimental procedure in Section S4A). This sample suffers from positional disorder around one of the three 1,3-bib linkers in the asymmetric unit. The disorder and partial occupancies are shown in Figure S22.

Alert Level B

PLAT341_ALERT_3_B Low Bond Precision on C-C Bonds ..... 0.01829 Ang.

Response: **sql-(1,3-bib)(ndc)-Ni-beta_vacuum** was prepared through **sql-(1,3-bib)(ndc)-Ni-beta**, i.e. by exchanging the as-synthesized sample **sql-(1,3-bib)(ndc)-Ni-alpha** with methanol and heating under vacuum, which triggered two subsequent structural transformations. As a result, the crystal quality was impacted. This was reflected in a B level alert related to low bond precision, which we attribute to poor diffraction. The reduced crystal quality of this sample can also be attributed to the fact that the crystal was glued to a glass rod inside a capillary, and part of the glue may have interfered with the diffraction.

PLAT601_ALERT_2_B Unit Cell Contains Solvent Accessible VOIDS of . 133 Ang**3

Response: **sql-(1,3-bib)(ndc)-Ni-beta_vacuum** was prepared through **sql-(1,3-bib)(ndc)-Ni-beta**, which adsorbs water molecules from the atmosphere. Even though the crystal was heated at 60 ˚C under vacuum overnight, guest water molecules were present in the crystal structure and were successfully modelled in two locations (O1A and O1B). However, the residual water molecule was not located. We therefore attribute the solvent accessible voids to a residual water molecule, as also found in the crystal structure of **sql-(13-bib)(ndc)-Ni-beta**.

sql-(bib)(ndc)-Ni-α'. Four H_2O guest molecules per Ni unit found in seven different positions were modelled anisotropically. Half an H_2O molecule (O1A) was found hydrogen-bonding to the aqua ligand, similar to the crystal structures of **α**, **γ** and **β**, and was refined anisotropically. This is a crystal has an inversion twin and, even though the appropriate twin law was employed, the Flack parameter is still slightly higher than the acceptable value for determination of absolute structure (0.35).

Alert Level B

PLAT417_ALERT_2_B Short Inter D-H..H-D H1B ..H1BA . 2.09 Ang.

Response: The atom O1B from a hydrate water molecule in **sql-(1,3-bib)(ndc)-Ni-alpha_prime** is hydrogen bonded to the coordinated O1 atom belonging to an aqua ligand, therefore causing a short intermolecular distance. This alert checks for intermolecular H...H distances of less than 1.8 Angstroms. In our case, the distance is 2.09 Angstroms therefore suggesting that our hydrogen bonding network is plausible.

S5. Powder X-ray Diffraction Measurements

Powder X-ray diffraction data was collected on crushed microcrystalline samples. Diffractograms were recorded using a PANalytical Empyrean™ diffractometer equipped with a PIXcel3D detector, operating in scanning line detector mode with an active length of 4 utilizing 255 channels, in the Continuous Scanning mode with the goniometer in the theta-theta orientation. The diffractometer is fitted with an Empyrean Cu LFF (long fine-focus) HR (9430 033 7310x) tube operated at 40 kV and 40 mA, and CuKα radiation (λα = 1.540598 Å) was used for diffraction experiments. Incident beam optics included the Fixed Divergences slit

with anti-scatter slit PreFIX module, with a 1/8° divergence slit and a 1/4° anti-scatter slit, as well as a 10 mm fixed incident beam mask and a Soller slit (0.04 rad). Divergent beam optics included a P7.5 anti-scatter slit, a Soller slit (0.04 rad), and a Ni-β filter. The data was collected from 4°-40° (2θ) with a step-size of 0.016413° and a varied scan time of 30-200 seconds per step.

S6. Variable-Temperature Powder X-ray Diffraction Measurements

Diffractograms at different temperatures were recorded using a PANalytical X'Pert Pro-MPD diffractometer equipped with a PIXcel3D detector, operating in scanning line detector mode with an active length of 4 utilizing 255 channels. Anton Paar TTK 450 stage coupled with the Anton Paar TCU 110 Temperature Control Unit were used to record the variable-temperature diffractograms. The diffractometer was outfitted with an Empyrean Cu LFF (long fine-focus) HR (9430 033 7300x) tube operated at 40 kV and 40 mA and CuKα radiation (λ = 1.54056 Å). Continuous scanning mode with the goniometer in the theta-theta orientation was used to collect the data. Incident beam optics included a 1/4° divergence slit and a Soller slit (0.04 rad). Divergent beam optics included a P7.5 anti-scatter slit, a Soller slit (0.04 rad) and a Ni-β filter. In a typical experiment, *ca.* 20 mg of sample was crushed to microcrystalline powder and was loaded on a zero background sample holder made for the Anton Paar TTK 450 chamber. Each sample was heated up to the noted temperature (no more than 200 ˚C) under N_2 atmosphere and then cooled back to room temperature. The data was collected from 3° to 35° (2θ) with a step-size of 0.016413° and a scan time of 200 seconds per step.

S7. *In situ* Powder X-ray Diffraction Measurements

In situ CO_2 loading PXRD experiments between 0 and 1 bar were recorded using a PANalytical X'Pert Pro MPD diffractometer equipped with a PIXcel3D detector. Anton Paar TTK 450 stage coupled with the Anton Paar TCU 110 Temperature Control Unit were used to record the gas loading experiments at a set temperature. The diffractometer was outfitted with an Empyrean Cu LFF (long fine-focus) HR (9430 033 7300x) tube operated at 40 kV and 40 mA and CuKα radiation (λ = 1.54056 Å). Continuous scanning mode with the goniometer in the theta-theta orientation was used to collect the data. Incident beam optics included a 1/4° divergence slit and a Soller slit (0.04 rad). Divergent beam optics included a P7.5 anti-scatter slit, a Soller slit (0.04 rad) and a Ni-β filter. In a typical experiment, *ca.* 20 mg of sample was crushed to microcrystalline powder and was loaded on a zero background sample holder made for Anton Paar TTK 450 chamber. The sample was subsequently loaded with CO_2 gas and the pressure was monitored using a CG16K capsule dial gauge. Variable-pressure PXRD patterns were measured at a constant temperature of 298 K.

S8. Thermogravimetric Analysis (TGA) and Differential Scanning Calorimetry (DSC) Analysis

Thermogravimetric analysis (TGA) was performed using a TA Instruments Q50 system. Samples were loaded into aluminium sample pans and heated at 10 °C/min from room temperature to 550 °C under N_2 flow. Differential scanning calorimetry (DSC) analysis was

performed on a Q2000 TA Instruments system. Samples were loaded into aluminium sample pans with a pinhole on the lids. The experiments were performed at heating rate of 5 °C/min from room temperature up to 300 °C under N_2 atmosphere.

S9. Fourier Transformed Infrared (FTIR) Spectroscopy

Spectra were obtained by using a Perkin Elmer Spectrum 100 FTIR Spectrometer with ATR and Spotlight 200 FTIR microscope attachment. A small amount of powder microcrystalline sample was placed onto the ATR plate and the spectra were collected in the range of 4000-650 cm^{-1} with resolution of 0.5 cm^{-1}.

S10. Elemental Analysis

Analysis was performed using an Exeter Analytical CE 440 elemental analyser (University College Dublin, Microanalytical Laboratory). Elemental analysis measurements were challenging in the case of **sql-(1,3-bib)(ndc)-Ni-γ** and **sql-(1,3-bib)(ndc)-Ni-α'** because of the spontaneous loss of solvent molecules in air (methanol and water, respectively. In order to overcome this, the materials were transported in liquid and filtered for 5 minutes before the experiment. This may have caused slight discrepancies from the expected values due to incomplete or excessive drying.

S11. Gas Sorption Measurements

S11A. General Procedure

For gas sorption experiments, high-purity gases were used as received from BOC Gases Ireland: CO_2 (99.995%), N_2 (99.9995%%), CH_4 (99.9995%), C_2H_2 (98.5%), C_2H_4 (99.92%), C_2H_6 (99.0%). A Micromeritics 3Flex surface area and pore size analyzer 3500 was used for collecting the low-pressure sorption isotherms for CO_2 and N_2. The temperature at 77 K was maintained using a 4 L Dewar filled with liquid nitrogen. The temperature at 195 K was maintained using a 4 L Dewar filled with a dry ice-acetone mixture. Bath temperatures of 273 and 298 K were precisely controlled with a Julabo ME (v.2) recirculating control system containing a mixture of ethylene glycol and water. Before each gas sorption experiment, the freshly prepared samples of **sql-(1,3-bib)(ndc)-Ni-α** was placed in a quartz tube and activated under high vacuum at 60 ˚C on a Micromeritics SmartVacPrep for 12 hrs, to generate the activate phase **sql-(1,3-bib)(ndc)-Ni-β**, as confirmed by PXRD measurements (Section S3). All low-pressure gas sorption studies were performed on the activated phase **sql-(1,3-bib)(ndc)-Ni-β**.

S11B. IAST Selectivity Calculations

The selectivities for the adsorbate mixture composition of interest were calculated from the single component adsorption isotherms using Ideal Adsorbed Solution Theory (IAST).[8,9] Single-component adsorption isotherms for CO_2 and N_2 at 298 K were fitted to the Langmuir equation:

$$n(P) = q * \frac{kP}{1 + kP}$$

where: $n(P)$ is the uptake (mmol/g) as a function of pressure

P is the total pressure (bar) of the bulk gas at equilibrium with the adsorbed phase

q is the saturation uptake (mmol/g)

k is the affinity coefficient (bar^{-1})

Single-component adsorption isotherm for CH_4 at 298 K was fitted to the Henry equation:

$$n(P) = k * P$$

where: $n(P)$ is the uptake (mmol/g) as a function of pressure

P is the total pressure (bar) of the bulk gas at equilibrium with the adsorbed phase

k is Henry's coefficient ($mmol\ g^{-1}\ bar^{-1}$)

Then, mixed-gas fractional uptakes were calculated and the selectivity was obtained as follows:

$$S_{i/j} = \frac{(x_i/x_j)}{(y_i/y_j)}$$

where: $S_{i/j}$ is the selectivity

x_i and x_j are the mole fractions of components i and j in the adsorbed phase

y_i and y_j are the mole fractions of components i and j in the gas phase

Fitting parameters for the CO_2, N_2 and CH_4 isotherms (collected at 298 K) are listed in Table S7.

S12. Dynamic Vapour Sorption

Water vapour sorption isotherm determination was performed using Adventure Dynamic Vapour Sorption (DVS) instrument manufactured by Surface Measurement Systems. The instrument gravimetrically measured water vapour uptake using air as a carrier gas. Digital mass flow controllers regulated the flows of dry and saturated gases. Relative humidity was generated by precisely mixing dry and saturated gas flows in desired flow ratios which produced expected relative humidity. Pure water was used to generate water vapour for these measurements and the temperature was maintained at 300 K by enclosing the system in a temperature-controlled incubator. The mass of the sample was determined by a high resolution microbalance Ultrabalance Low Mass with a precision of 0.01 µg. The microbalance had symmetric configuration with two branches of the balance being exposed to the same gas and being kept at the same temperature, which allowed negation of buoyancy and drag effects. A flow of 400 sccm (Standard Cubic Centimetres per Minute) was used for the measurements at 300 K. Prior to the measurement, the sample was activated *in situ* in dry air at 358 K for 60 minutes using a built-in preheater and consequently cooled to sorption temperature in 90 minutes. Isotherm measurements were performed on approximately 12 mg of activated sample. For each isotherm point, $dm/dt < 0.01\ \%\ min^{-1}$ was used as criteria of reaching equilibrium.

Figures and Tables

Table S1. CNs that exhibit structural flexibility when exposed to water.

Compound	Dimensions	Shape of isotherm	Mechanism	Reference
$[Cu(tzc)(dpp)]_n$	1D	N/A	Removal/addition of the noncoordinating interchain water molecules	10
[Cu(bpetha)(2,2′-bpy)(MeOH)]·2PF6	1D	S-shaped	Changes in the coordination environment of Cu centres	11
$(NH_4)_3[Co_2(bamdpH)_2(HCOO)(H_2O)_2]$	1D	N/A	Changes in the coordination environment of Co centres	12
$[Zn(H_2SSA)_2(H_2O)_2]$	1D	S-shaped	Hydrolysis of Zn–sulfonate bonds	13
$[Zn(3\text{-}tba)_2]$	1D	S-shaped	Cleavage of bonds and hydrogen bonding	14
[Cu(HQS)(TMBP)]	1D	S-shaped	Ligand contortion	15
$[Co_2(bipy)_3(SO_4)_2(H_2O)_2](bipy)(CH_3OH)$	2D	N/A	Removal/addition of coordinated water molecules	16
$[Ce(tci)(H_2O)_2]$	2D	N/A	Bonding rearrangement	17
CID-5/CID-6	2D	S-shaped	Ligand rotation	18
NTU-19	2D	N/A	2D to 3D dimensionality conversion	19
MCID-1	2D	S-shaped	Layer expansion	20
UTSA-300-Cu	2D	N/A	Layer expansion	21
sql-(azpy)(pdia)-Ni	2D	S-shaped	Layer expansion	22
sql-(1,3-bib)(ndc)-Ni	**2D**	**S-shaped**	**Layer expansion and hydrogen bonding**	**this work**
MIL-53 Family	3D	S-shaped	Swelling	23-27
$[Cu_2(pzdc)_2(dpyg)]$	3D	N/A	N/A	28
CPL-2	3D	S-shaped	Ligand rotation	29
MIL-88 Family	3D	S-shaped	Swelling	30, 31
$[Mn(NNdmenH)(H_2O)][Cr(CN)_6]$	3D	S-shaped	Removal/addition of coordinated water molecules	32
$Ba_3(H_2O)_3(L)_2(H_2O)_8$	3D	N/A	Changes in the coordination environment of Ba centres	33
Cu(BDTri)L	3D	N/A	Breathing	34
AEMOF-1	3D	N/A	N/A	35

BP	3D	S-shaped	Co(II) ions from tetrahedral to octahedral; framework from neutral to cationic	[36]
[Zn(4-bpdh)(DHT)]	3D	No uptake	N/A	[37]
SHF-61	3D	N/A	Breathing	[38]
BUT-8(Cr)A	3D	S-shaped	"Knee-cap" ligand rotation	[39]
MUV-2	3D	N/A	Breathing	[40]
DUT-98	3D	S-shaped	Pore shrinkage	[41]
SIFSIX-23-Cu	3D	S-shaped	Ligand rotation/bending	[42]
$[Cu(HL)(DMSO)\cdot(MeOH)]_n$	3D	N/A	3D to 1D dimensionality conversion	[43]
JUK-8	3D	S-shaped	Breathing, hydrogen bonding	[44]
1Mn	3D	Multi-step	Change of the cyanide bridging pattern	[45]
ZPF-2-Co	3D	S-shaped	Ligand rotation	[46]
X-dia-2-Cd	3D	S-shaped	Ligand rotation	[47]

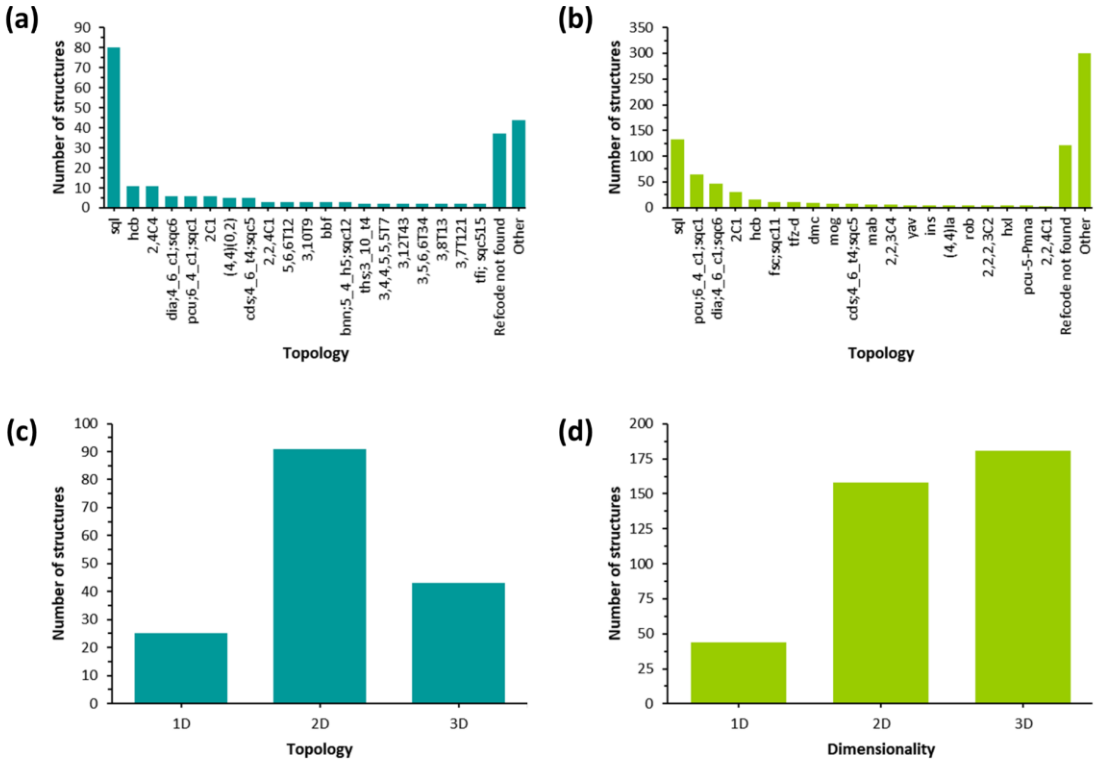

Figure S1. Topology (a and b) and dimensionality (c and d) results of the twenty most frequent topologies in CNs sustained by 1,3-bib (cyan) and 1,4-bib (blue), respectively.

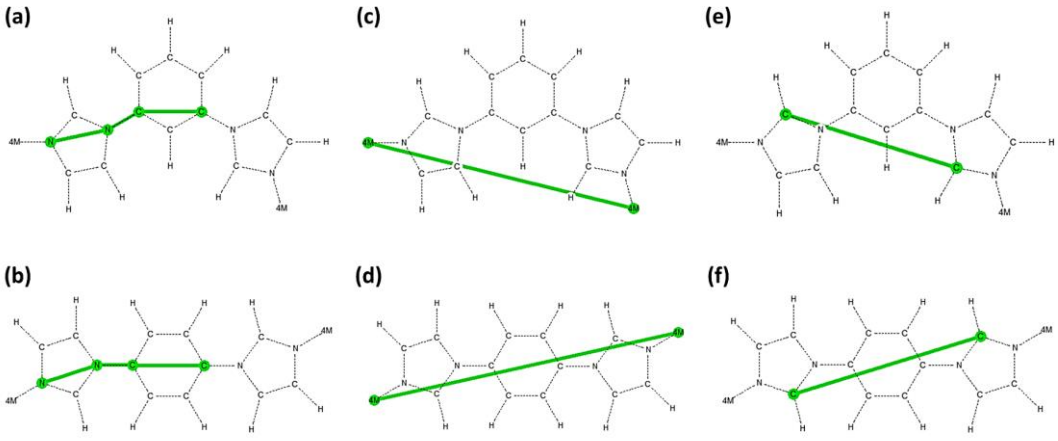

Figure S2. Search using the ConQuest function of the CSD database: torsion angle between the imidazole ring and the central phenyl ring (a and b), metal-to-metal (M-M) distance (c and d) and carbon-to-carbon (C-C) distance between the two 2- position carbon atoms of the imidazole rings (e and f) for 1,3-bib (top) and 1,4-bib (bottom), respectively.

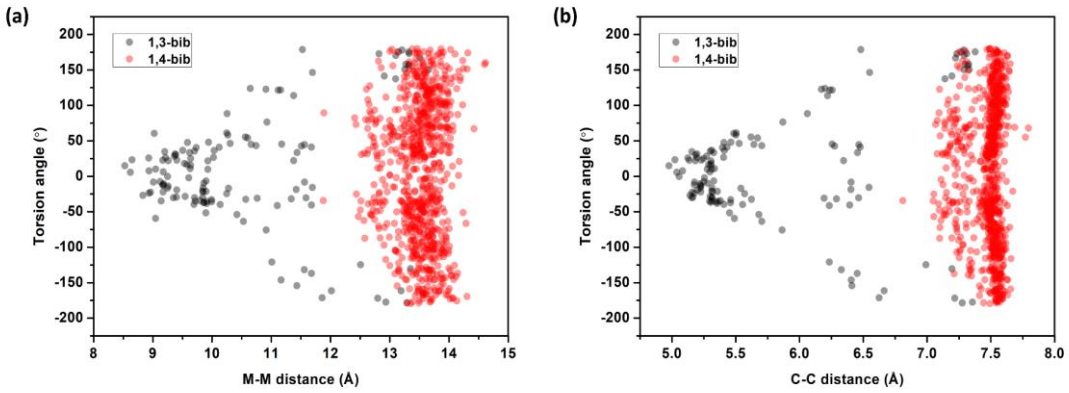

Figure S3. Outcome of a CSD search for 1,3-bib (black) and 1,4-bib (red): torsion angle with respect to M-M distance (a) and C-C distance (b). The relevant parameters are depicted in Figure S2.

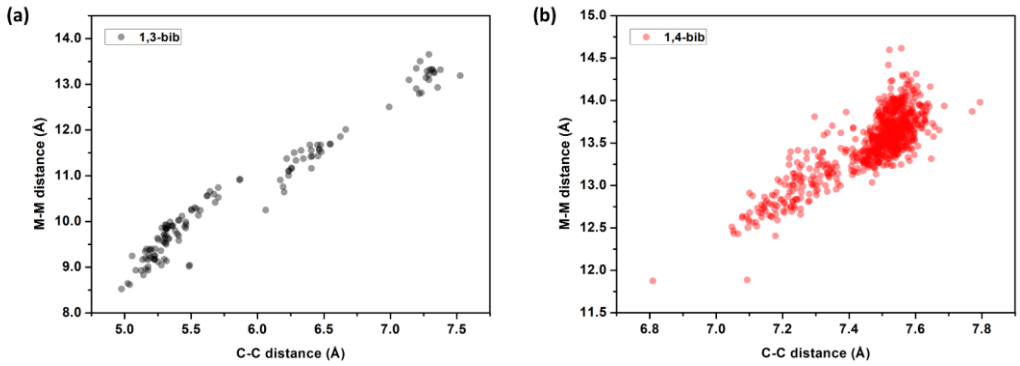

Figure S4. Outcome of a CSD search for 1,3-bib (a, black) and 1,4-bib (b, red): M-M distance with respect to C-C distance. The relevant parameters are depicted in Figure S2.

According to Figure S4, the plot of M-M vs. C-C distance in 1,3-bib can be divided in three clusters, depending on the configuration of the ligand (from left to right): *syn-endo*, *anti*, *syn-exo*. On the contrary, 1,4-bib can only exist in two configurations, *syn* or *anti*, which result in two custers of M-M vs. C-C distance results (Figure S4). The configurations of the two linkers are shown in Figure S5.

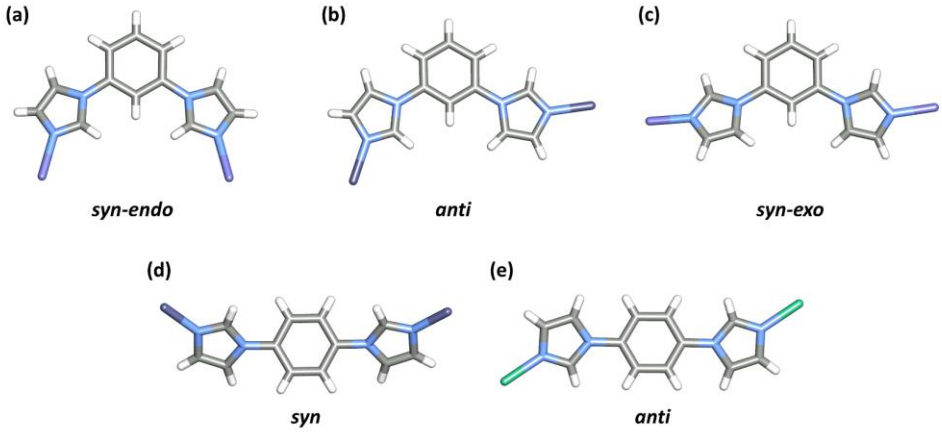

Figure S5. Linker configurations for 1,3-bib (top) and 1,4-bib (bottom) taken from reported examples with the following CSD refcodes: (a) SOZQAB, (b) GIPNUR, (c) ZAHLIH, (d) YIJLAH and (e) SEVXEZ.

Table S2. Crystallographic information and refinement parameters for **sql-(1,3-bib)(ndc)-Ni**.

Compound	**sql-(1,3-bib)(ndc)-Ni-α**	**sql-(1,3-bib)(ndc)-Ni-γ**
Formula	$[C_{30}H_{23}N_6NiO_5]\cdot$[+solvent]	$[C_{30}H_{23}N_6NiO_5]\cdot$[+solvent]
Formula weight	692.43	727.53
Temperature (K)	150.00	150.00
Crystal system	Orthorhombic	Orthorhombic
Space group	$Cmc2_1$	$Cmc2_1$
a (Å)	21.9995(8)	22.0063(17)
b (Å)	14.6850(5)	16.5739(13)
c (Å)	19.4382(6)	18.9230(14)
α (°)	90	90
β (°)	90	90
γ (°)	90	90
V (Å^3)	6279.8(4)	6901.8(9)
Z	8	8
D_c (g·cm^{-3})	1.465	1.400
μ (mm^{-1})	0.681	0.624
R_{int}	0.0416	0.0845
GOF	1.046	1.049
R_1 [I > 2σ (I)]	0.0331	0.0738
WR_2 [all data]	0.0877	0.2290
Diff peak / hole (e Å^{-3})	0.672 / -0.571	0.959 / -0.541
No. CCDC	2288421	2288422

Table S2 (continued). Crystallographic information and refinement parameters for **sql-(1,3-bib)(ndc)-Ni**.

Compound	sql-(1,3-bib)(ndc)-Ni-β	sql-(1,3-bib)(ndc)-Ni-β _vacuum	sql-(1,3-bib)(ndc)-Ni-α'
Formula	$[C_{30}H_{23}N_6NiO_5]\cdot$[+solvent]	$[C_{30}H_{23}N_6NiO_5]\cdot$ [+solvent]	$[C_{30}H_{23}N_6NiO_5]\cdot$[+solvent]
Formula weight	624.77	624.77	670.12
Temperature (K)	150.00	150.00	150.00
Crystal system	Orthorhombic	Orthorhombic	Orthorhombic
Space group	$Cmc2_1$	$Cmc2_1$	$Cmc2_1$
a (Å)	21.9277(15)	21.925(4)	21.9932(12)
b (Å)	13.3810(9)	13.614(3)	14.6091(8)
c (Å)	19.9622(13)	19.848(3)	19.5808(12)
α (°)	90	90	90
β (°)	90	90	90
γ (°)	90	90	90
V (Å^3)	5857.2(7)	5924.5(18)	6291.3(6)
Z	8	8	8
D_c (g·cm^{-3})	1.417	1.401	1.415
μ (mm^{-1})	0.716	0.708	1.421
R_{int}	0.0500	0.0951	0.0823
GOF	1.015	1.042	1.093
R_1 [I > 2σ (I)]	0.0418	0.0796	0.0813
WR_2 [all data]	0.1001	0.2344	0.2440
Diff peak / hole (e Å^{-3})	0.759 / -0.533	1.285 / -0.632	0.988 / -0.658
No. CCDC	2288423	2288424	2288425

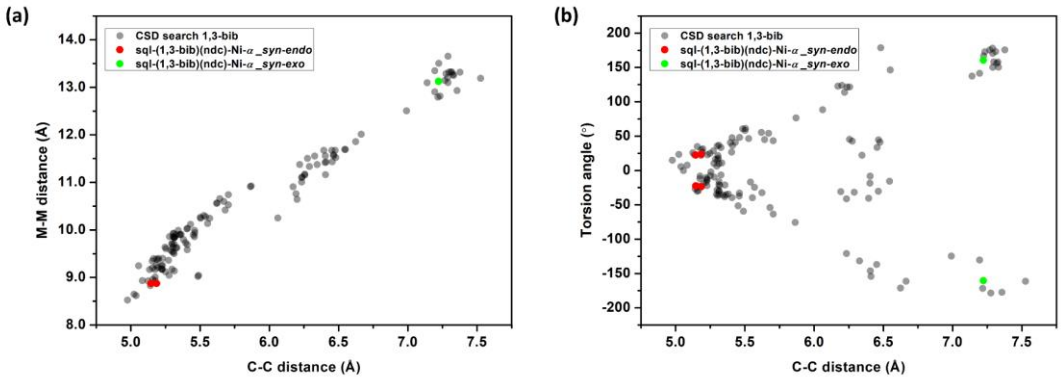

Figure S6. Outcome of a CSD search for 1,3-bib (black) and comparison with the 1,3-bib configurations (red and green) in **sql-(1,3-bib)(ndc)-Ni-α**: M-M distance with respect to C-C distance (a) and torsion angle with respect to C-C distance (b). The relevant parameters are depicted in Figure S2.

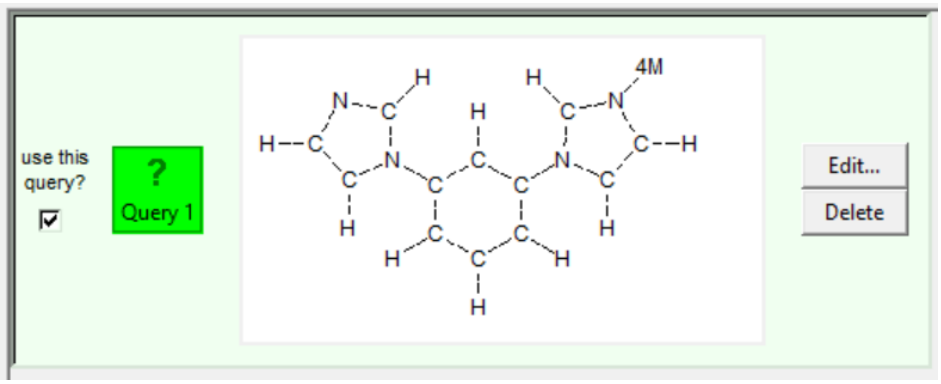

Figure S7. Snapshot of the ConQuest query base on the ligand 1,3-bib.

Table S3. Outcome of a CSD survey including the query in Figure S7. This table includes all examples where an $M_2(1,3\text{-bib})_2$ loop coordination pattern was found. Single linker: N-donor linker (1,3-bib); mixed linker: N-donor linker (1,3-bib) combined with O-donor linker.

No.	Refcode	Dimension	Linker Type	Reference
	KINCES	0D	single linker	48
	KINCIW			
	KINCOC			
	LAYFEY	0D		49
	MIJKAU	0D		50
	MIJSIK			
	MOLDOI	0D		51
	NECSEU	0D		52
	ODOCUH	0D		53
	ROKKIO	0D		54
	VIBVUZ	0D		55
	VIBWAG			
	VIBWEK			
	WOMCEI	0D		56
	ZUFCAG	0D		57
	EJUREG	1D	single linker	58
	FOZWIC	1D		59
	FUHFIZ	1D		
	LAYFIC	1D		49
	PIWGIN	1D		60
	SOSZAD	1D		61
	KOVYIG	2D	mixed linker	62
	KUHPUB	2D		63
	LAYFUO	2D		49
	UMODUY	2D		64
	WOMCAE	2D	single linker	56
	GINKOG	3D	mixed linker	65
	ZIDPUA	3D		66

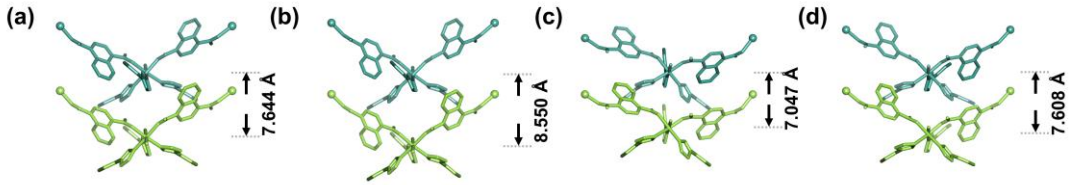

Figure S8. Internetwork Ni···Ni distances in **sql-(1,3-bib)(ndc)-Ni-α** (a), **sql-(1,3-bib)(ndc)-Ni-γ** (b), **sql-(1,3-bib)(ndc)-Ni-β** (c) and **sql-(1,3-bib)(ndc)-Ni-α'** (d) along the crystallographic *c* axis.

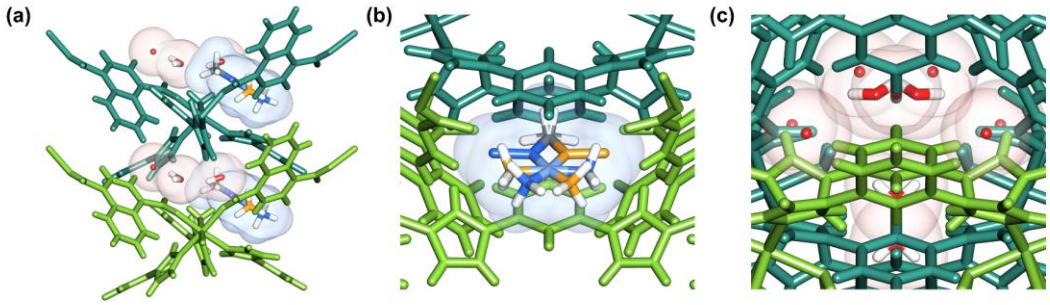

Figure S9. Guest molecules in **sql-(1,3-bib)(ndc)-Ni-α** (a), 2-fold disordered *N,N*-dimethylacetamide molecules in blue spaces (b) and water molecules in red spaces (c).

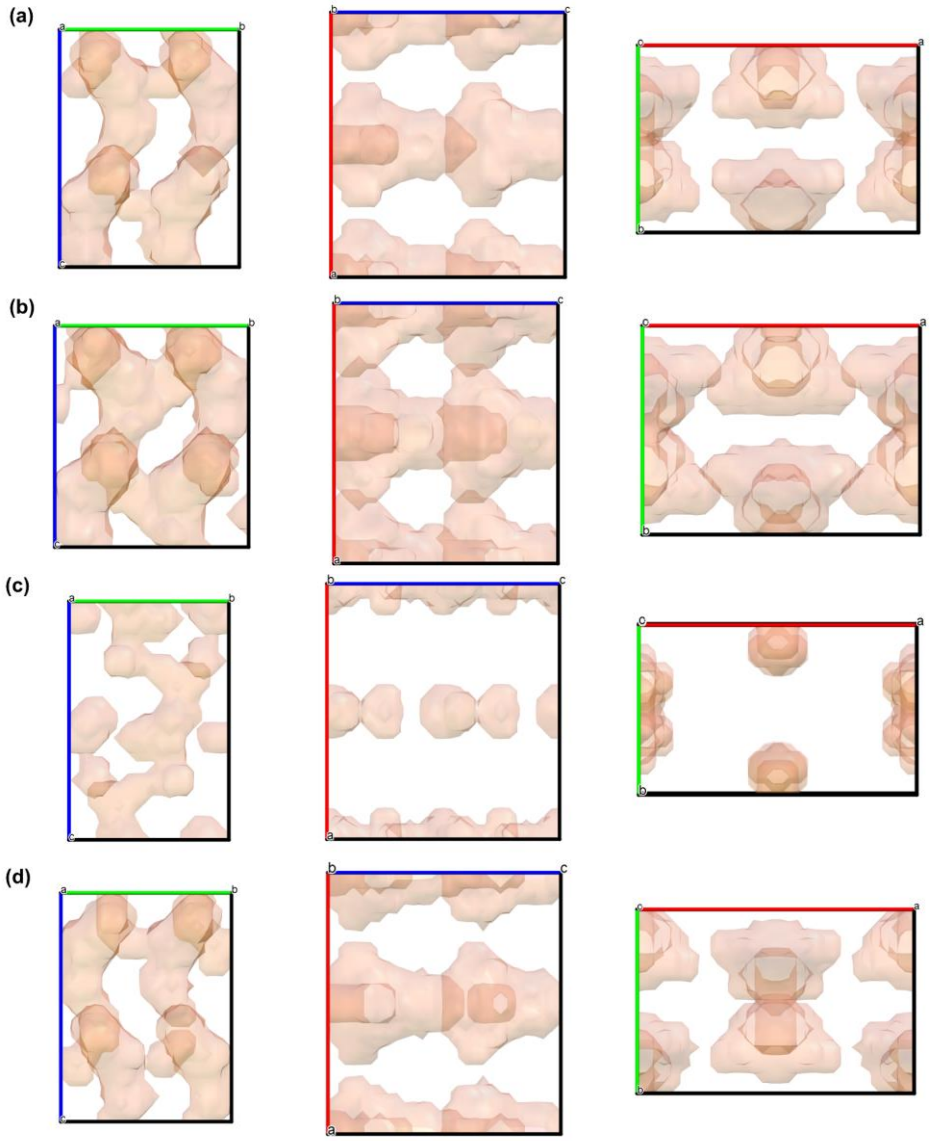

Figure S10. Guest accessible space in **sql-(1,3-bib)(ndc)-Ni-α** (a), **sql-(1,3-bib)(ndc)-Ni-γ** (b), **sql-(1,3-bib)(ndc)-Ni-β** (c) and **sql-(1,3-bib)(ndc)-Ni-α'** (d) along the crystallographic *a* (left), *b* (middle) and *c* (right) axis. The guest accessible space was calculated with a probe radius of 1.2 Å, without removing the hydrogen bonded water molecule shown in Figure S12.

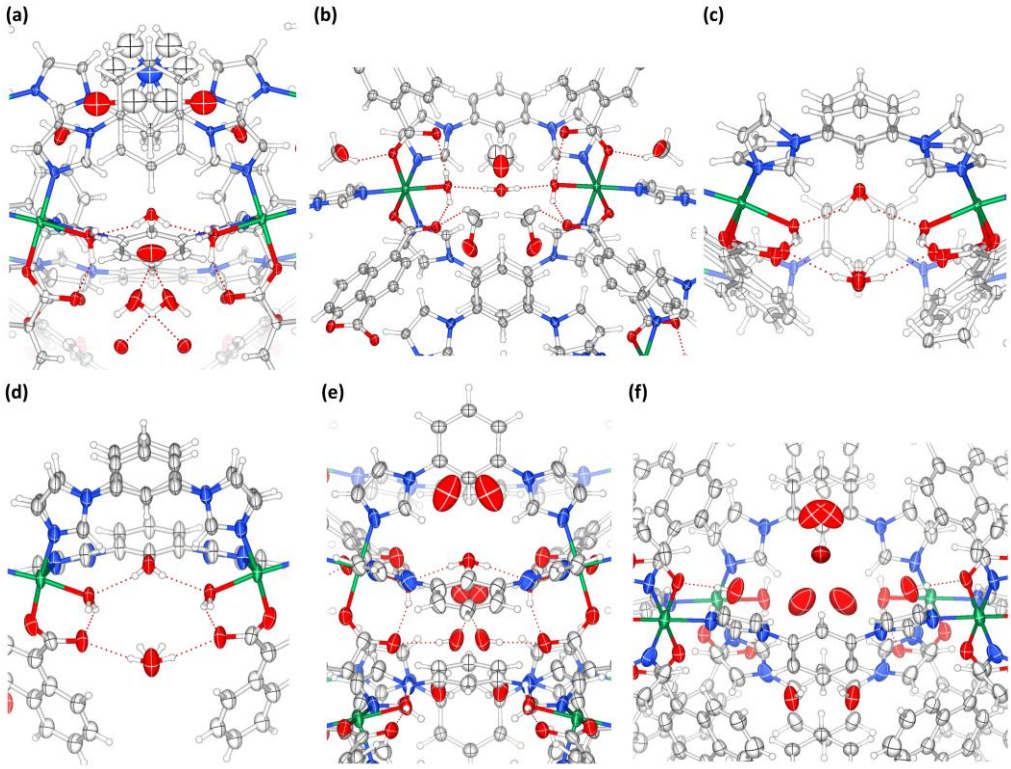

Figure S11. Atomic displacement parameters (ADPs) displayed at a 50 percent probability level for **sql-(1,3-bib)(ndc)-Ni-α** (a), **sql-(1,3-bib)(ndc)-Ni-γ** (b), **sql-(1,3-bib)(ndc)-Ni-β** (c), **sql-(1,3-bib)(ndc)-Ni-β_vacuum** (d) and **sql-(1,3-bib)(ndc)-Ni-α'** (e and f).

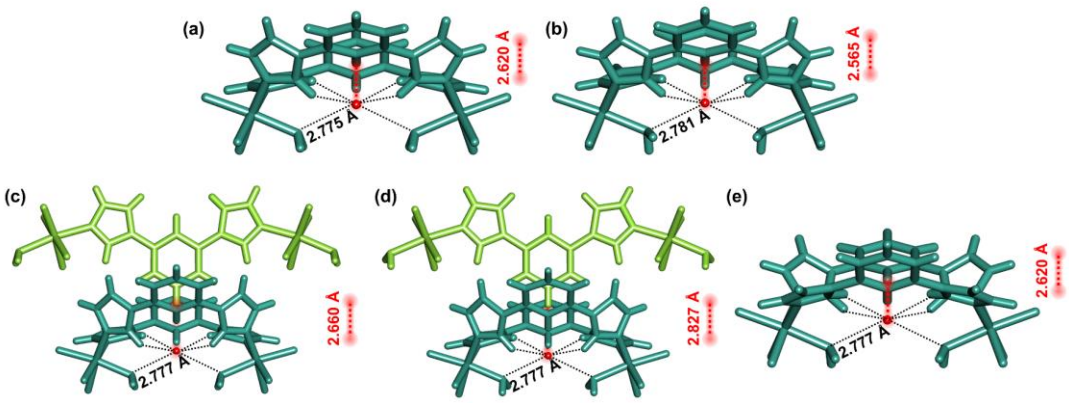

Figure S12. Short contact distances (O···O and O···H) between a guest water molecule and the framework in **sql-(1,3-bib)(ndc)-Ni-α** (a), **sql-(1,3-bib)(ndc)-Ni-γ** (b), **sql-(1,3-bib)(ndc)-Ni-β** (c), **sql-(1,3-bib)(ndc)-Ni-β_vacuum** (d) and **sql-(1,3-bib)(ndc)-Ni-α'** (e).

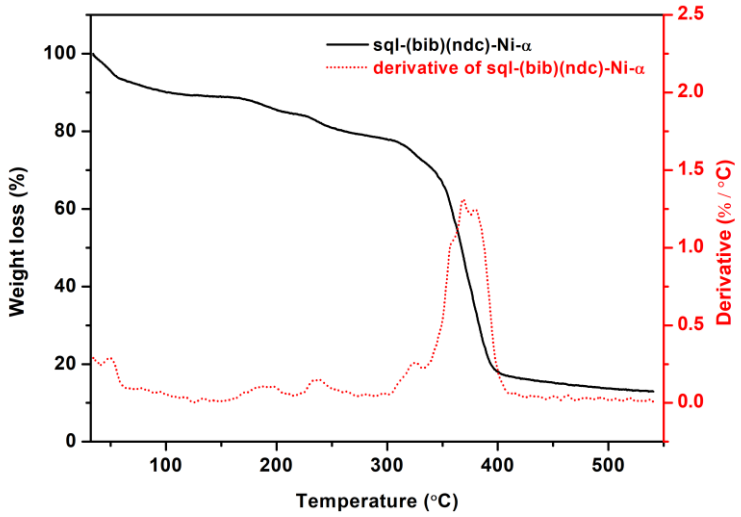

Figure S13. TG curve (black) and derivative of weight loss as a function of temperature (red) of **sql-(1,3-bib)(ndc)-Ni-α** under N_2 environment.

As shown in Figure S13, **sql-(1,3-bib)(ndc)-Ni-α** displayed a weight loss of 15.8% completed at 225 °C, corresponding to the release of half a DMA molecule and two H_2O molecules per Ni unit (calc. 11.5%), followed by a 4.8% weight loss completed by 250 °C, corresponding to the release of half a hydrogen bonded H_2O molecule (see Figure S12) and one coordinated H_2O molecule per Ni unit (calc. 3.9%).

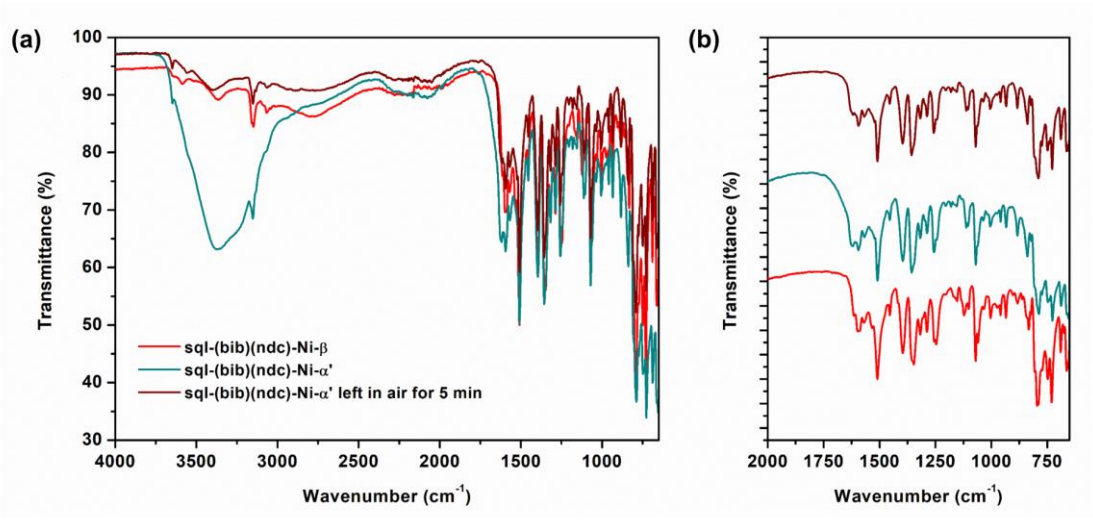

Figure S14. FTIR spectra of **sql-(1,3-bib)(ndc)-Ni-β** (bright red), **sql-(1,3-bib)(ndc)-Ni-α'** (cyan) and **sql-(1,3-bib)(ndc)-Ni-α'** left in air (50% RH) for five minutes (dark red) recorded in the range of 4000 to 650 cm^{-1} (a) and magnified overlay of the spectra in the range of 2000 to 650 cm^{-1} (b).

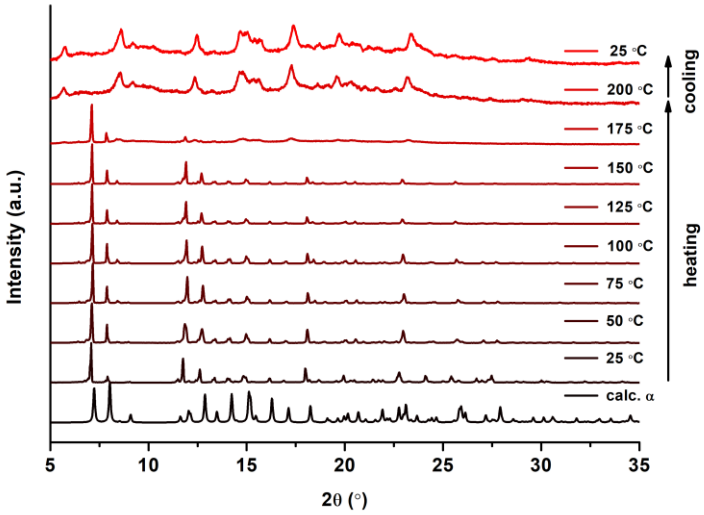

Figure S15. *In situ* variable temperature PXRD patterns of **sql-(1,3-bib)(ndc)-Ni-α** under N_2 flow.

As shown in Figure S15, **sql-(1,3-bib)(ndc)-Ni-α** did not undergo phase change upon heating. At 200 ˚C, when the guest molecules were removed, the compound became amorphous, as indicated by the broad peaks and low signal to noise ratio in the PXRD at 200 ˚C.

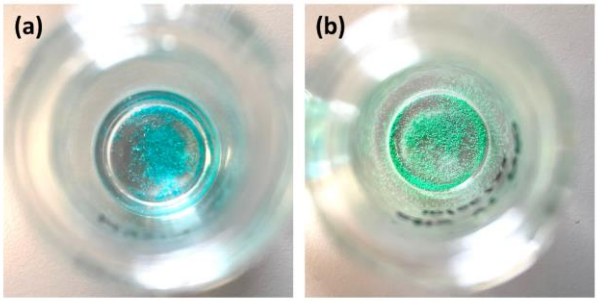

Figure S16. Colour change induced by VT-PXRD: (a) as-synthesised **sql-(1,3-bib)(ndc)-Ni-α** and (b) **sql-(1,3-bib)(ndc)-Ni-α** after heating up to 200 ˚C during VT-PXRD studies.

The change in sample colour from blue to green (Figure S16) indicated that the decomposition could have been triggered by loss of coordinated aqua ligands and subsequent changes to the coordination environment of the Ni centres occurring close to the boiling point of DMA.

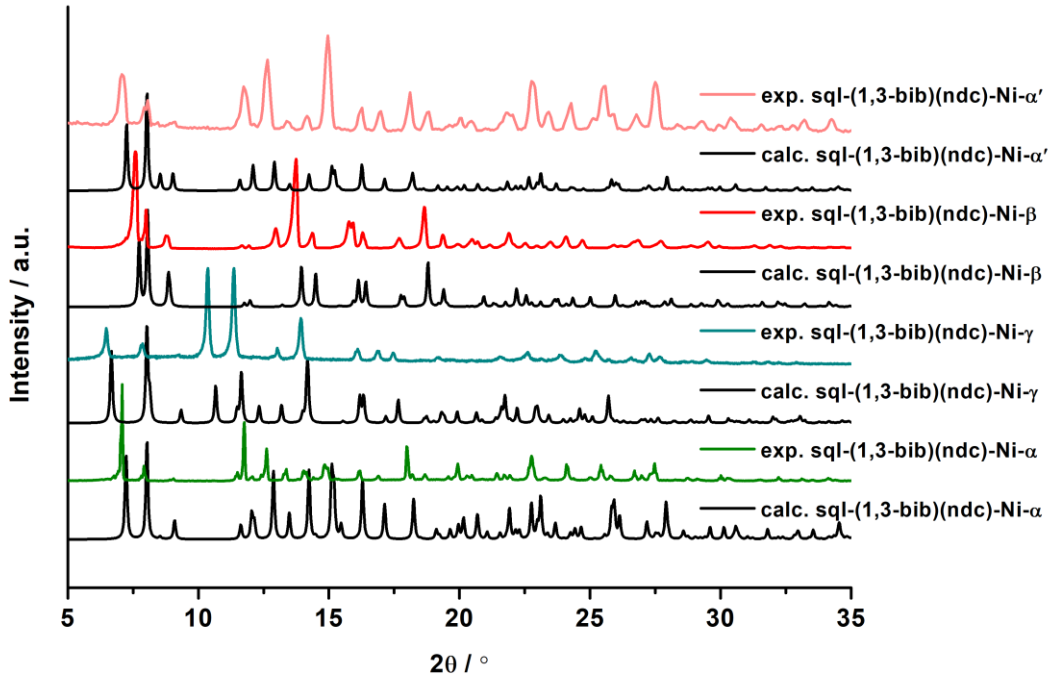

Figure S17. Calculated and experimental PXRD patterns of **sql-(1,3-bib)(ndc)-Ni-α**, **sql-(1,3-bib)(ndc)-Ni-γ**, **sql-(1,3-bib)(ndc)-Ni-β** and **sql-(1,3-bib)(ndc)-Ni-α'**.

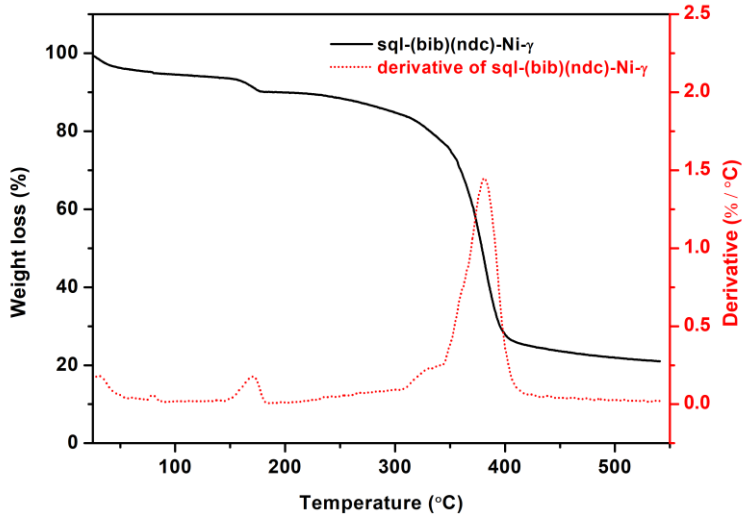

Figure S18. TG curve (black) and derivative of weight loss as a function of temperature (red) of **sql-(1,3-bib)(ndc)-Ni-γ** under N_2 environment.

As shown in Figure S18, **sql-(1,3-bib)(ndc)-Ni-γ** displayed a weight loss of 7.6% completed at 100 °C, corresponding to the release of two MeOH molecules per Ni unit (calc. 9.4%). The weight loss completed at *ca.* 200 °C indicated the presence of half a hydrogen bonded H_2O guest molecule (see Figure S12) and one coordinated H_2O molecule (exp. 3.0%, calc. 2.6%).

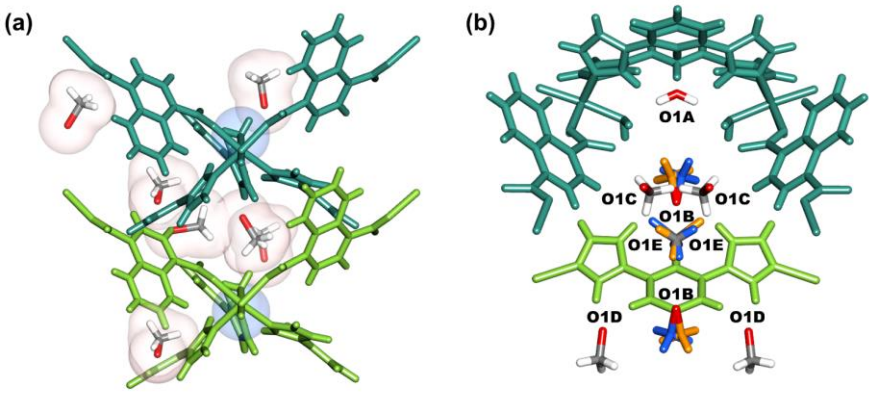

Figure S19. Guest molecules in **sql-(1,3-bib)(ndc)-Ni-γ**, with water molecules shown in blue spaces and methanol molecules shown in red spaces (a); labelled guest molecules with disorder shown in orange and blue (b).

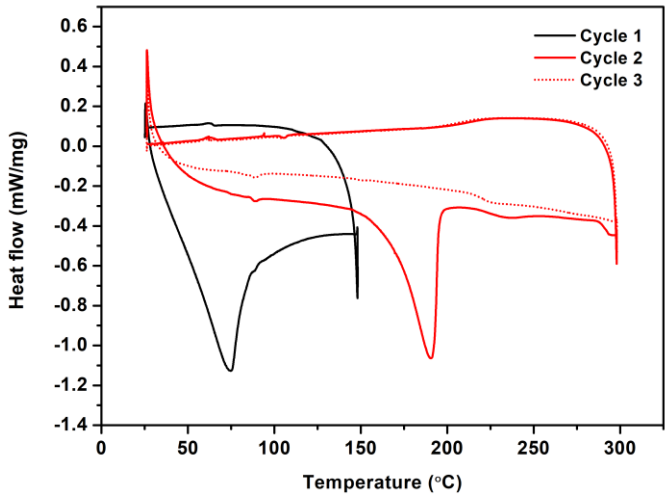

Figure S20. DSC profile of **sql-(1,3-bib)(ndc)-Ni-γ** for two consecutive cycles (cycle 1, black line; cycle 2, red solid line; cycle 3, red dotted line).

As shown in Figure S20, heating **sql-(1,3-bib)(ndc)-Ni-γ** up to 150 ˚C (cycle 1) indicated a phase change to **sql-(1,3-bib)(ndc)-Ni-β**. During cycle 2, the absence of the phase change peak showed that the resulting **sql-(1,3-bib)(ndc)-Ni-β** remained stable after conversion. Instead, a peak was observed at *ca.* 180 ˚C, which is consistent with the removal of the hydrogen-bonded H_2O molecule between two Ni centres, and subsequent framework collapse. This is in agreement with recorded TGA data (Figure S18). Cycle 3 revealed the absence of the peaks observed in cycles 1 and 2, consistent with framework decomposition.

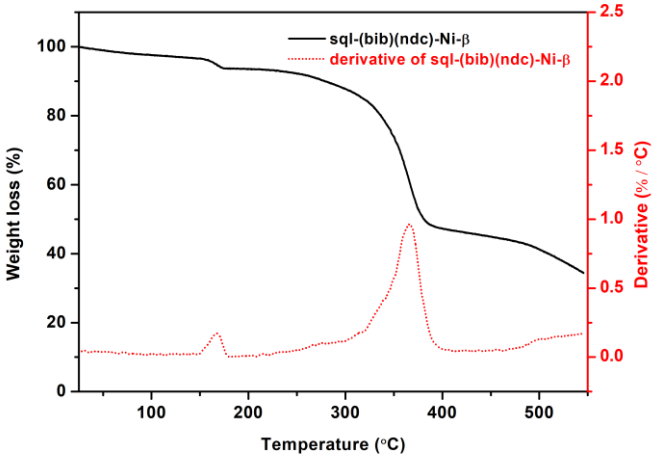

Figure S21. TG curve (black) and derivative of weight loss as a function of temperature (red) of **sql-(1,3-bib)(ndc)-Ni-β** under N_2 environment.

As shown in Figure S20, **sql-(1,3-bib)(ndc)-Ni-β** displayed a weight loss of 3.1% completed at 100 °C, corresponding to the release of one H_2O guest molecule per Ni unit (calc. 2.8%). The weight loss at *ca.* 150 °C indicated the presence of and half a hydrogen bonded H_2O molecule (Figure S12) and one coordinated H_2O molecule per Ni unit (exp. 3.5%, calc. 4.3%).

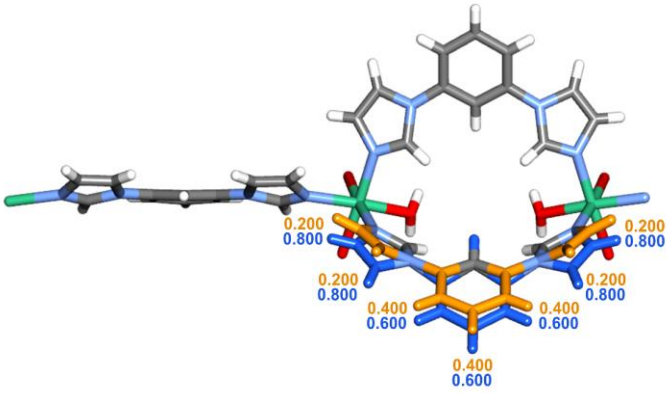

Figure S22. Disorder of the ligand 1,3-bib and partial occupancies in the crystal structure of **sql-(1,3-bib)(ndc)-Ni-β_vacuum**.

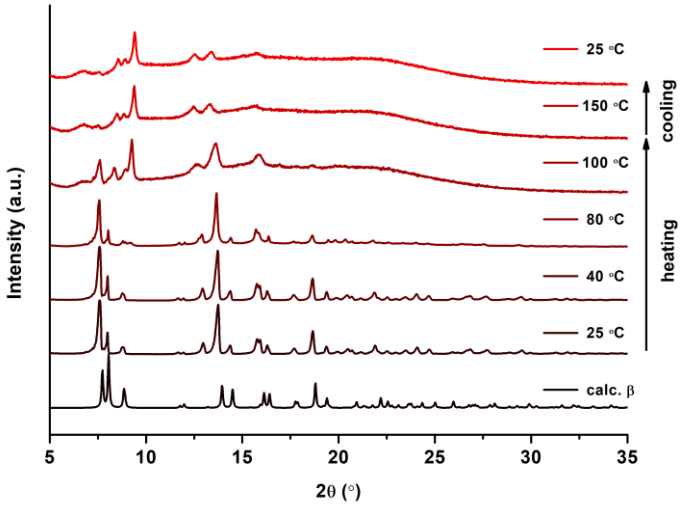

Figure S23. *In situ* variable-temperature PXRD patterns of **sql-(1,3-bib)(ndc)-Ni-β** under vacuum.

As shown in Figure S23, upon heating of **sql-(1,3-bib)(ndc)-Ni-β** in the absence of moisture (under vacuum), decomposition was completed at *ca.* 150 ˚C, possibly with removal of the coordinated water molecules which induced a colour change from blue to green (Figure S16). This is in agreement with TGA data (Figure S21).

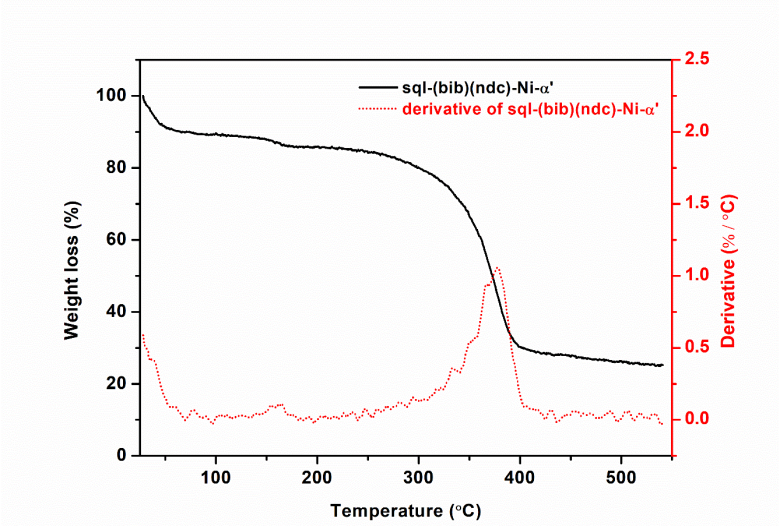

Figure S24. TG curve (black) and derivative of weight loss as a function of temperature (red) of **sql-(1,3-bib)(ndc)-Ni-α'** under N_2 environment.

As shown in Figure S24, **sql-(1,3-bib)(ndc)-Ni-α'** displayed a weight loss of 10.8% completed at 100 °C, corresponding to the release of three and a half H_2O molecules per Ni unit (calc. 9.3%). The weight loss completed at *ca.* 200 °C indicated the presence of half a hydrogen bonded H_2O guest molecule (Figure S12) and one coordinated H_2O molecule per Ni unit (exp. 3.0%, calc. 3.9%).

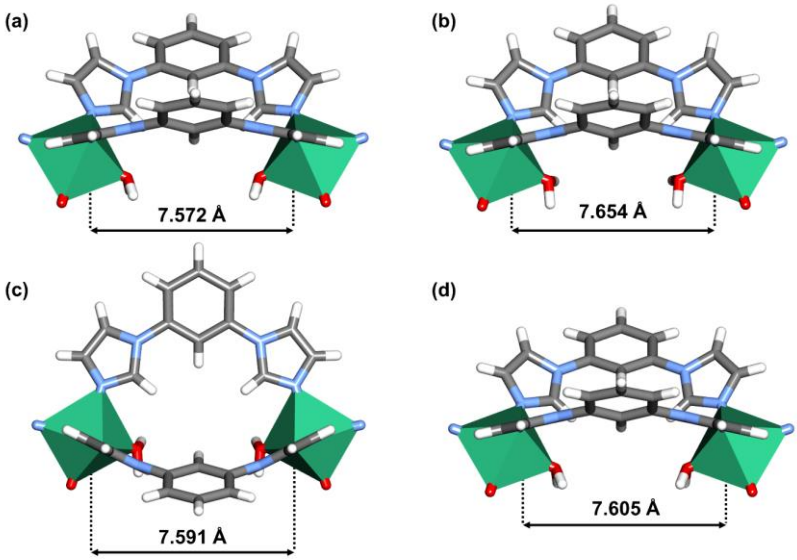

Figure S25. Conformation of the 1,3-bib ligand and N···N distances along the crystallographic *c* axis in **sql-(1,3-bib)(ndc)-Ni-α** (a), **sql-(1,3-bib)(ndc)-Ni-γ** (b), **sql-(1,3-bib)(ndc)-Ni-β** (c) and **sql-(1,3-bib)(ndc)-Ni-α'** (d).

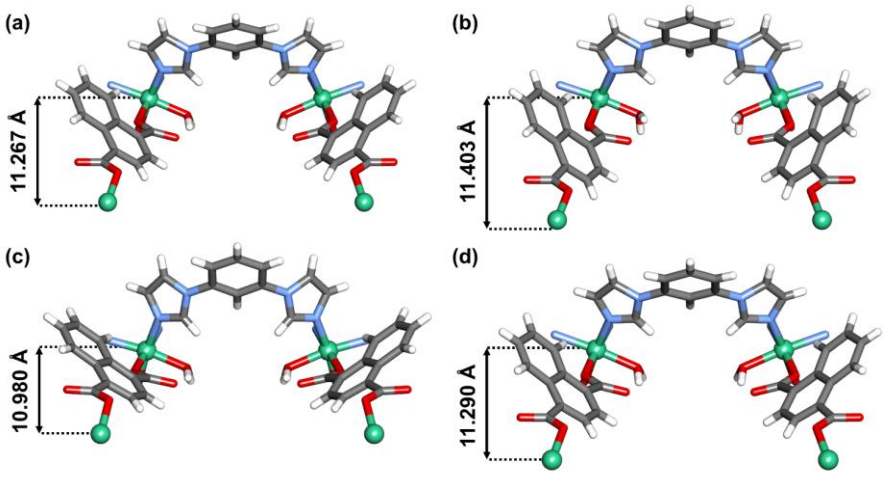

Figure S26. Conformation of the ndc ligand and Ni···Ni distances along the crystallographic *c* axis in **sql-(1,3-bib)(ndc)-Ni-α** (a), **sql-(1,3-bib)(ndc)-Ni-γ** (b), **sql-(1,3-bib)(ndc)-Ni-β** (c) and **sql-(1,3-bib)(ndc)-Ni-α'** (d).

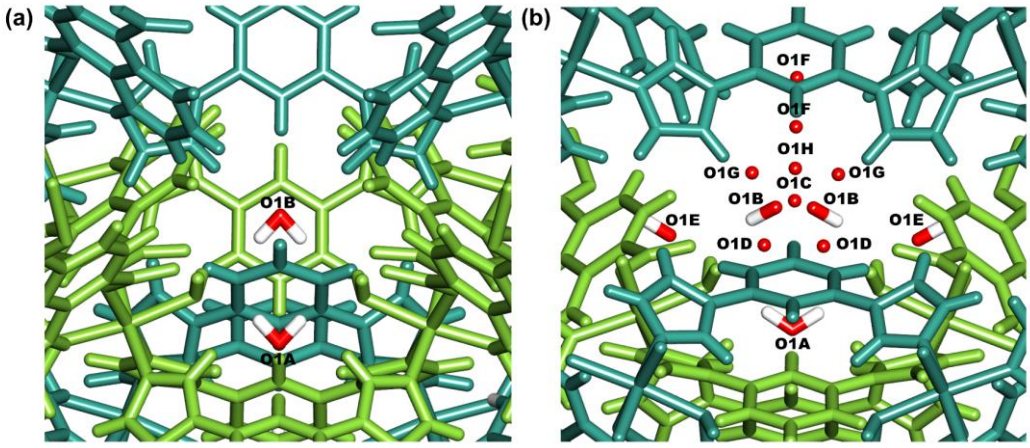

Figure S27. Host-guest interactions in **sql-(1,3-bib)(ndc)-Ni-β** (a) and **sql-(1,3-bib)(ndc)-Ni-α'** (b).

Table S4. List of interactions of the guest water molecules in **sql-(1,3-bib)(ndc)-Ni-α'**.

Interaction	Distance (Å)	Framework/Guest Interaction
O1A···O1	2.777	Aqua ligand
O1A···H5	2.620	Phenyl ring of 1,3-bib ligand
O1A···H8	2.535	Imidazole ring of 1,3-bib ligand
O1B···H17	2.551	Imidazole ring of 1,3-bib ligand
O1B···O3	2.979	Uncoordinated O atom of ndc ligand
O1B···O1C	2.681	Network of H_2O guest molecules
O1B···O1G	2.148	Network of H_2O guest molecules
O1C···H6	2.604	Phenyl ring of 1,3-bib ligand
O1C···O1F	2.597	Network of H_2O guest molecules
O1D···O1E	2.820	Network of H_2O guest molecules
O1E···H15	2.554	Imidazole ring of 1,3-bib ligand
O1E···O5	2.791	Uncoordinated O atom of ndc ligand
O1F···H19	2.610	Phenyl ring of 1,3-bib ligand
O1F···H27	2.534	Phenyl ring of ndc ligand
O1F···O1H	2.997	Network of H_2O guest molecules
O1G···H26	2.658	Phenyl ring of ndc ligand
O1G···O1H	2.846	Network of H_2O guest molecules

Table S5. List of interactions of the guest water molecules in **sql-(1,3-bib)(ndc)-Ni-β**.

Interaction	Distance (Å)	Framework/Guest Interaction
O1A···O1	2.777	Aqua ligand
O1A···H1	2.435	Imidazole ring of 1,3-bib ligand
O1A···H12	2.498	Phenyl ring of 1,3-bib ligand
O1A···H20	2.660	Phenyl ring of 1,3-bib ligand
O1B···H17	2.568	Imidazole ring of 1,3-bib ligand
O1B···O4	2.975	Uncoordinated O atom of ndc ligand

Figure S28. Temperature (a, left) and humidity (b, right) readings for the PXRD patterns of **sql-(1,3-bib)(ndc)-Ni-β** collected in air (top) and in liquid water (bottom). The PXRD patterns are shown in Figure 3 in the main text.

Table S6. Calculated water uptake from experimental single crystal data for **sql-(1,3-bib)(ndc)-Ni-β** and **sql-(1,3-bib)(ndc)-Ni-α'**. The hydrogen bonded water molecule (see Figure 10) was omitted from the calculation.

Compound	Single Crystal Uptake (molecules per Ni unit)	Single Crystal Uptake (cm^3/g)	Uptake from DVS Experiment (cm^3/g)
sql-(1,3-bib)(ndc)-Ni-β	0.9	32.0	38.6, at RH = 30%
sql-(1,3-bib)(ndc)-Ni-α'	3.2	107.4	101.3, at RH = 95%

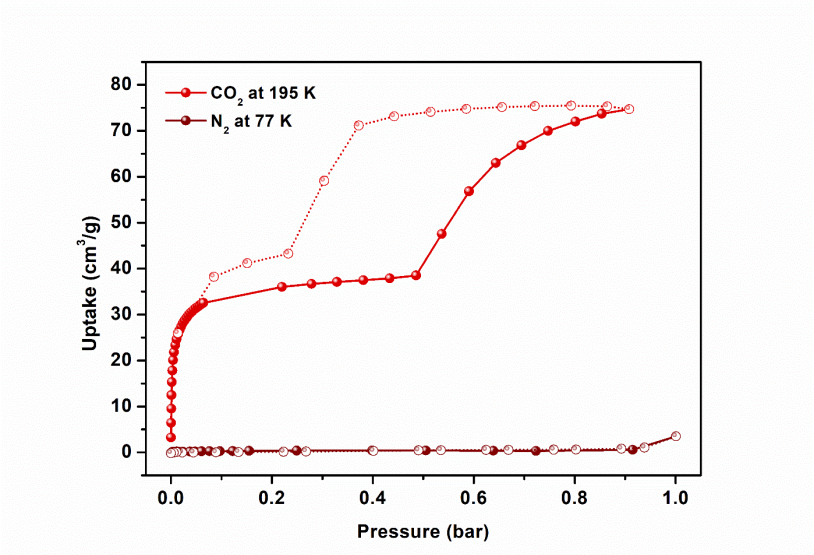

Figure S29. CO_2 (bright red) and N_2 (dark red) gas sorption isotherms for **sql-(1,3-bib)(ndc)-Ni** collected at cryogenic temperatures, *i.e.* 195 K and 77 K for CO_2 and N_2, respectively. Adsorption = full sphere; desorption = open sphere.

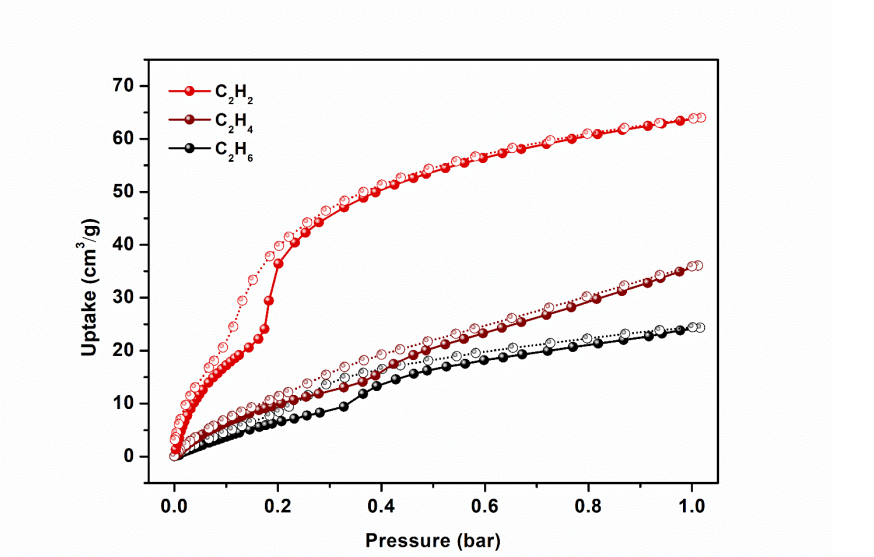

Figure S30. C_2H_2 (bright red), C_2H_4 (dark red) and C_2H_6 (black) gas sorption isotherms for **sql-(1,3-bib)(ndc)-Ni** collected at 273 K. Adsorption = full sphere; desorption = open sphere.

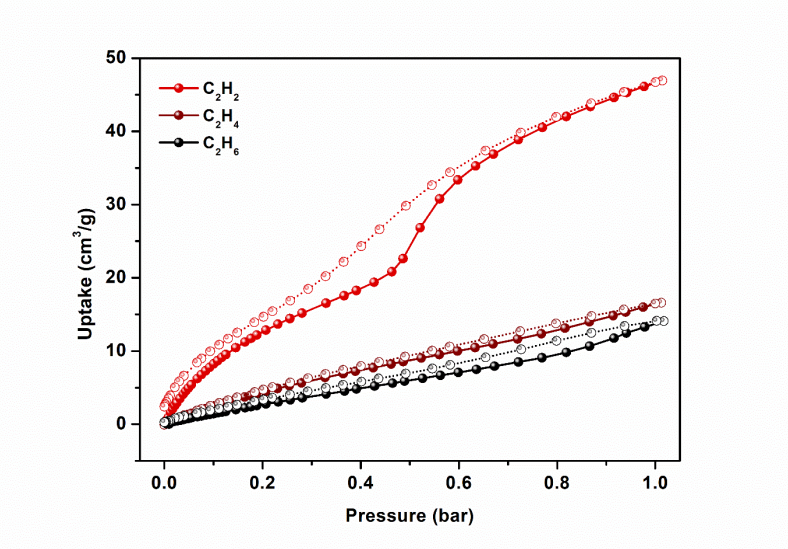

Figure S31. C_2H_2 (bright red), C_2H_4 (dark red) and C_2H_6 (black) gas sorption isotherms for **sql-(1,3-bib)(ndc)-Ni** collected at 298 K. Adsorption = full sphere; desorption = open sphere.

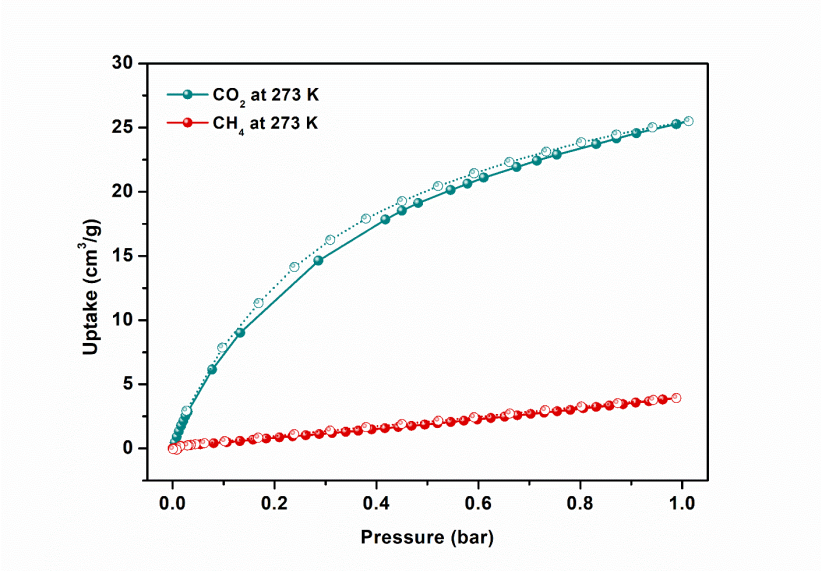

Figure S32. CO_2 (cyan) and CH_4 (red) gas sorption isotherms for **sql-(1,3-bib)(ndc)-Ni** collected at 273 K. Adsorption = full sphere; desorption = open sphere.

Table S7. Isotherm fitting parameters and fit values for IAST calculations.

Adsorbent	Adsorbate	Model	R^2	q (mmol/g)	k (bar^{-1})
sql-(1,3-bib)(ndc)-Ni-β	CO_2	Langmuir	0.999959	1.23735	1.48919
	N_2		0.976715	0.276452	0.283192
	Adsorbate	**Model**	**R^2**	**k ($mmol\ g^{-1}bar^{-1}$)**	
	CH_4	Henry	0.995509	0.0848703	

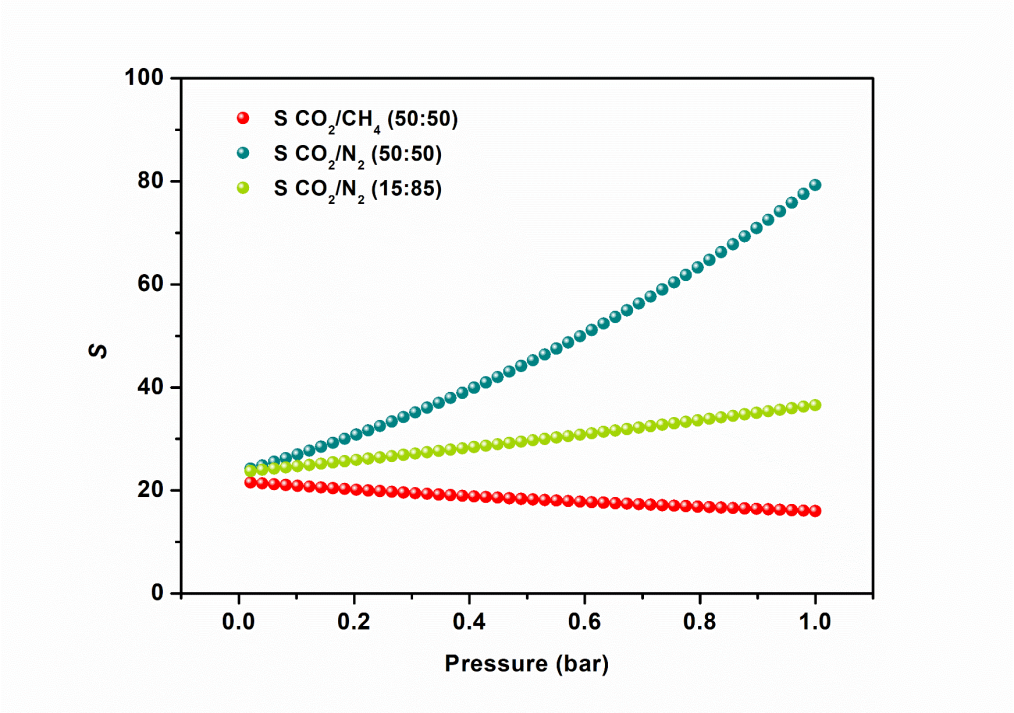

Figure S33. IAST selectivities of **sql-(1,3-bib)(ndc)-Ni-β** at 298 K for CO_2/N_2 and compositions of 15:85 (green) and 50:50 (cyan) or CO_2/CH_4 and composition of 50:50 (red), plotted as a function of pressure.

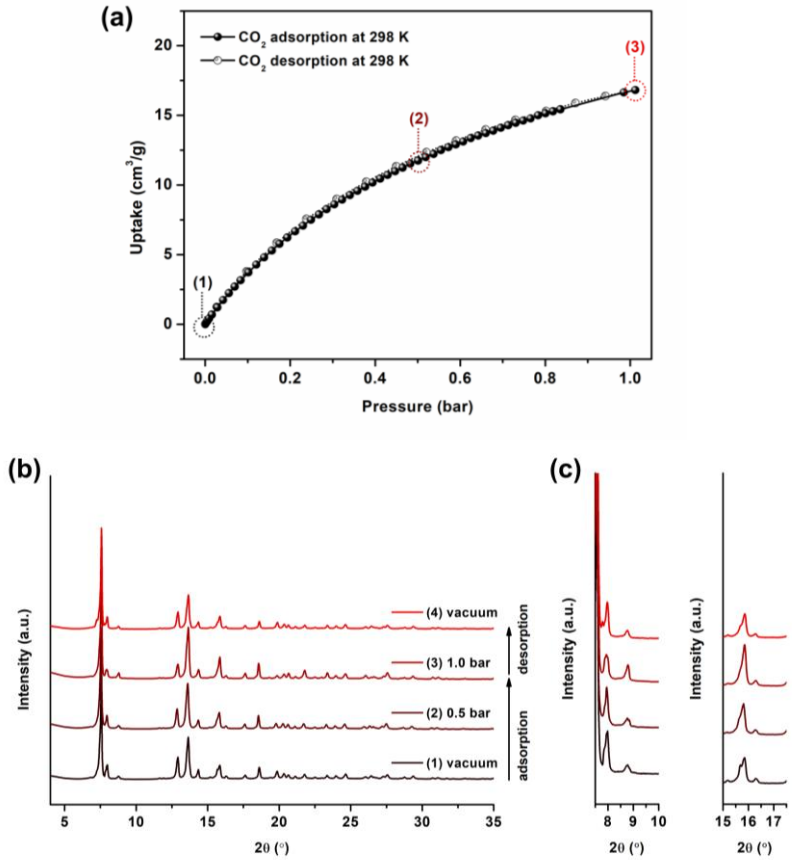

Figure S34. (a) CO_2 gas sorption isotherm for **sql-(1,3-bib)(ndc)-Ni** collected at 298 K; (b) *in situ* CO_2-loaded PXRD patterns at 0, 0.5 and 1.0 bar collected at 298 K and (c) magnified *in situ* PXRD patterns in the regions 7.5 to 10 ˚ and 15 to 17.5 ˚ 2θ.

As shown in Figure S34, the peaks at *ca.* 9˚ and 16˚ 2θ increased in intensity with subsequent loading, and eventually decreased after desorption to match the starting PXRD pattern.

References

1. R. H. Lam, S. T. Keaveney, B. A. Messerle and I. Pernik, *ACS Catalysis*, 2023, **13**, 1999-2010.
2. W.-G. Jia, L.-L. Gao, Z.-B. Wang, L.-Y. Sun and Y.-F. Han, *Organometallics*, 2019, **38**, 1946-1954.
3. I. J. Bruno, J. C. Cole, P. R. Edgington, M. Kessler, C. F. Macrae, P. McCabe, J. Pearson and R. Taylor, *Acta Crystallographica Section B*, 2002, **58**, 389-397.
4. V. A. Blatov, A. P. Shevchenko and D. M. Proserpio, *Crystal Growth & Design*, 2014, **14**, 3576-3586.
5. T. Francart, A. van Wieringen and J. Wouters, *J Neurosci Methods*, 2008, **172**, 283-293.
6. G. Sheldrick, *Inc.: Madison, WI*, 2008.
7. O. V. Dolomanov, L. J. Bourhis, R. J. Gildea, J. A. K. Howard and H. Puschmann, *Journal of Applied Crystallography*, 2009, **42**, 339-341.
8. A. L. Myers and J. M. Prausnitz, *AIChE Journal*, 1965, **11**, 121-127.
9. K. S. Walton and D. S. Sholl, *AIChE Journal*, 2015, **61**, 2757-2762.
10. M. Wriedt, A. A. Yakovenko, G. J. Halder, A. V. Prosvirin, K. R. Dunbar and H.-C. Zhou, *Journal of the American Chemical Society*, 2013, **135**, 4040-4050.
11. S.-i. Noro, K. Fukuhara, K. Kubo and T. Nakamura, *Crystal Growth & Design*, 2011, **11**, 2379-2385.
12. Z.-S. Cai, S.-S. Bao, X.-Z. Wang, Z. Hu and L.-M. Zheng, *Inorganic Chemistry*, 2016, **55**, 3706-3712.
13. J. H. Song, D. W. Kim, D. W. Kang, W. R. Lee and C. S. Hong, *Chemical Communications*, 2019, **55**, 9713-9716.
14. M. Deng, S. Mukherjee, Y.-J. Liang, X.-D. Fang, A.-X. Zhu and M. J. Zaworotko, *Chemical Communications*, 2022, **58**, 8218-8221.
15. M. Shivanna, A. A. Bezrukov, V. Gascón-Pérez, K.-i. Otake, S. Sanda, D. J. O'Hearn, Q.-Y. Yang, S. Kitagawa and M. J. Zaworotko, *ACS Applied Materials & Interfaces*, 2022, **14**, 39560-39566.
16. D. Bradshaw, J. E. Warren and M. J. Rosseinsky, *Science*, 2007, **315**, 977-980.
17. S. K. Ghosh, J.-P. Zhang and S. Kitagawa, *Angewandte Chemie International Edition*, 2007, **46**, 7965-7968.
18. T. Fukushima, S. Horike, Y. Inubushi, K. Nakagawa, Y. Kubota, M. Takata and S. Kitagawa, *Angewandte Chemie International Edition*, 2010, **49**, 4820-4824.
19. H. Wang, H. Cao, J.-j. Zheng, S. Mathew, N. Hosono, B. Zhou, H. Lyu, S. Kusaka, W. Jin, S. Kitagawa and J. Duan, *Chemistry – A European Journal*, 2018, **24**, 6412-6417.
20. Y. Kamakura, A. Hikawa, H. Yoshikawa, W. Kosaka, H. Miyasaka and D. Tanaka, *Chemical Communications*, 2020, **56**, 9106-9109.
21. J. Wang, Y. Zhang, P. Zhang, J. Hu, R.-B. Lin, Q. Deng, Z. Zeng, H. Xing, S. Deng and B. Chen, *Journal of the American Chemical Society*, 2020, **142**, 9744-9751.
22. X. Li, D. Sensharma, V. I. Nikolayenko, S. Darwish, A. A. Bezrukov, N. Kumar, W. Liu, X.-J. Kong, Z. Zhang and M. J. Zaworotko, *Chemistry of Materials*, 2023, **35**, 783-791.
23. F. Millange, C. Serre and G. Férey, *Chemical Communications*, 2002, DOI: 10.1039/B201381A, 822-823.
24. C. Serre, F. Millange, C. Thouvenot, M. Noguès, G. Marsolier, D. Louër and G. Férey, *Journal of the American Chemical Society*, 2002, **124**, 13519-13526.
25. T. Loiseau, C. Serre, C. Huguenard, G. Fink, F. Taulelle, M. Henry, T. Bataille and G. Férey, *Chemistry – A European Journal*, 2004, **10**, 1373-1382.
26. S. Bourrelly, B. Moulin, A. Rivera, G. Maurin, S. Devautour-Vinot, C. Serre, T. Devic, P. Horcajada, A. Vimont, G. Clet, M. Daturi, J.-C. Lavalley, S. Loera-Serna, R. Denoyel, P.

L. Llewellyn and G. Férey, *Journal of the American Chemical Society*, 2010, **132**, 9488-9498.
27. A. Shigematsu, T. Yamada and H. Kitagawa, *Journal of the American Chemical Society*, 2011, **133**, 2034-2036.
28. R. Kitaura, K. Fujimoto, S.-i. Noro, M. Kondo and S. Kitagawa, *Angewandte Chemie International Edition*, 2002, **41**, 133-135.
29. R. Matsuda, R. Kitaura, S. Kitagawa, Y. Kubota, T. C. Kobayashi, S. Horike and M. Takata, *Journal of the American Chemical Society*, 2004, **126**, 14063-14070.
30. C. Mellot-Draznieks, C. Serre, S. Surblé, N. Audebrand and G. Férey, *Journal of the American Chemical Society*, 2005, **127**, 16273-16278.
31. J. Troyano, A. Carné-Sánchez, J. Pérez-Carvajal, L. León-Reina, I. Imaz, A. Cabeza and D. Maspoch, *Angewandte Chemie International Edition*, 2018, **57**, 15420-15424.
32. W. Kaneko, M. Ohba and S. Kitagawa, *Journal of the American Chemical Society*, 2007, **129**, 13706-13712.
33. B. D. Chandler, G. D. Enright, K. A. Udachin, S. Pawsey, J. A. Ripmeester, D. T. Cramb and G. K. H. Shimizu, *Nature Materials*, 2008, **7**, 229-235.
34. A. Demessence and J. R. Long, *Chemistry – A European Journal*, 2010, **16**, 5902-5908.
35. A. Douvali, A. C. Tsipis, S. V. Eliseeva, S. Petoud, G. S. Papaefstathiou, C. D. Malliakas, I. Papadas, G. S. Armatas, I. Margiolaki, M. G. Kanatzidis, T. Lazarides and M. J. Manos, *Angewandte Chemie International Edition*, 2015, **54**, 1651-1656.
36. Q. Chen, Z. Chang, W.-C. Song, H. Song, H.-B. Song, T.-L. Hu and X.-H. Bu, *Angewandte Chemie International Edition*, 2013, **52**, 11550-11553.
37. B. Bhattacharya, A. Halder, L. Paul, S. Chakrabarti and D. Ghoshal, *Chemistry – A European Journal*, 2016, **22**, 14998-15005.
38. E. J. Carrington, C. A. McAnally, A. J. Fletcher, S. P. Thompson, M. Warren and L. Brammer, *Nature Chemistry*, 2017, **9**, 882-889.
39. F. Yang, G. Xu, Y. Dou, B. Wang, H. Zhang, H. Wu, W. Zhou, J.-R. Li and B. Chen, *Nature Energy*, 2017, **2**, 877-883.
40. M. Souto, J. Romero, J. Calbo, I. J. Vitórica-Yrezábal, J. L. Zafra, J. Casado, E. Ortí, A. Walsh and G. Mínguez Espallargas, *Journal of the American Chemical Society*, 2018, **140**, 10562-10569.
41. S. Krause, V. Bon, H. C. Du, R. E. Dunin-Borkowski, U. Stoeck, I. Senkovska and S. Kaskel, *Beilstein J. Nanotechnol.*, 2019, **10**, 1737-1744.
42. B.-Q. Song, Q.-Y. Yang, S.-Q. Wang, M. Vandichel, A. Kumar, C. Crowley, N. Kumar, C.-H. Deng, V. GasconPerez, M. Lusi, H. Wu, W. Zhou and M. J. Zaworotko, *Journal of the American Chemical Society*, 2020, **142**, 6896-6901.
43. S. Nakatsuka, Y. Watanabe, Y. Kamakura, S. Horike, D. Tanaka and T. Hatakeyama, *Angewandte Chemie International Edition*, 2020, **59**, 1435-1439.
44. K. Roztocki, F. Formalik, A. Krawczuk, I. Senkovska, B. Kuchta, S. Kaskel and D. Matoga, *Angewandte Chemie International Edition*, 2020, **59**, 4491-4497.
45. M. Magott, B. Gaweł, M. Sarewicz, M. Reczyński, K. Ogorzały, W. Makowski and D. Pinkowicz, *Chemical Science*, 2021, **12**, 9176-9188.
46. M. Yang, S.-Q. Wang, Z. Liu, Y. Chen, M. J. Zaworotko, P. Cheng, J.-G. Ma and Z. Zhang, *Journal of the American Chemical Society*, 2021, **143**, 7732-7739.
47. A. Subanbekova, V. I. Nikolayenko, A. A. Bezrukov, D. Sensharma, N. Kumar, D. J. O'Hearn, V. Bon, S.-Q. Wang, K. Koupepidou, S. Darwish, S. Kaskel and M. J. Zaworotko, *Journal of Materials Chemistry A*, 2023, **11**, 9691-9699.
48. S. Ganta, R. Jagan and D. K. Chand, *Inorganica Chimica Acta*, 2019, **484**, 33-41.
49. L. Schlechte, V. Bon, R. Grünker, N. Klein, I. Senkovska and S. Kaskel, *Polyhedron*, 2012, **44**, 179-186.

50. Q. Wu, L.-Y. Liu, S. Li, F.-X. Wang, J. Li, Y. Qian, Z. Su, Z.-W. Mao, P. J. Sadler and H.-K. Liu, *Journal of Inorganic Biochemistry*, 2018, **189**, 30-39.
51. D. Samanta and P. S. Mukherjee, *Chemistry – A European Journal*, 2014, **20**, 12483-12492.
52. W.-D. Xu and M.-H. Shu, *Acta Crystallographica Section E*, 2006, **62**, m3341-m3342.
53. S. Yuan, H. Wang, D.-X. Wang, H.-F. Lu, S.-Y. Feng and D. Sun, *CrystEngComm*, 2013, **15**, 7792-7802.
54. J. Li, Y. Y. Hao, Y. Qian, X. L. Xue, Z. Su and H. K. Liu, *Chinese Journal of Inorganic Chemistry*, 2019, **35**, 1500-1508.
55. L. Qin, Z. Pan, L. Qian, Y. Li, Z. Guo and H. Zheng, *CrystEngComm*, 2013, **15**, 5016-5019.
56. J. Pang, F. Jiang, D. Yuan, J. Zheng, M. Wu, G. Liu, K. Su and M. Hong, *Chemical Science*, 2014, **5**, 4163-4166.
57. S. Ganta and D. K. Chand, *Dalton Transactions*, 2015, **44**, 15181-15188.
58. S. U. Son, K. H. Park, B. Y. Kim and Y. K. Chung, *Crystal Growth & Design*, 2003, **3**, 507-512.
59. C. Zhang, Z. Zhang, Y. Guo, H. Liu, H. Ma, B. Liu, H. Pang and S. Li, *Structural Chemistry*, 2016, **27**, 439-447.
60. T. Yu, K. Wang, H. Ma, H. Pang and S. Li, *RSC Advances*, 2014, **4**, 2235-2241.
61. D. Wu, K. Wang, H. Ma, H. Pang, T. Yu, Z. Zhang, S. Li and H. Liu, *Solid State Sciences*, 2014, **35**, 39-44.
62. M. L. Zhang, Y. J. Zheng, M. Liu, Y. X. Ren, J. J. Wang, H. L. Cui and L. Liu, *Chinese Journal of Inorganic Chemistry*, 2019, **35**, 1813-1820.
63. X. Zhang, H. Chen, B. Li, G. Liu and X. Liu, *CrystEngComm*, 2019, **21**, 1231-1241.
64. M.-L. Zhang, Y. Bai, Y.-X. Ren, J.-J. Wang, X.-G. Yang and L.-F. Ma, *CrystEngComm*, 2021, **23**, 1616-1627.
65. X.-T. Zhang, H.-T. Chen, B. Li, G.-Z. Liu and X.-Z. Liu, *Journal of Solid State Chemistry*, 2018, **267**, 28-34.
66. M.-L. Zhang, Y.-J. Zheng, Z.-Z. Ma, Y.-X. Ren and J.-J. Wang, *Polyhedron*, 2018, **154**, 473-479.